science.sciencemag.org/cgi/content/full/science.aaz7949/DC1

Supplementary Materials for

Emergence of complexity in hierarchically organized chiral particles

Wenfeng Jiang, Zhi-bei Qu, Prashant Kumar, Drew Vecchio, Yuefei Wang, Yu Ma, Joong Hwan Bahng, Kalil Bernardino, Weverson R. Gomes, Felippe M. Colombari, Asdrubal Lozada-Blanco, Michael Veksler, Emanuele Marino, Alex Simon, Christopher Murray, Sérgio Ricardo Muniz, André F. de Moura*, Nicholas A. Kotov*

*Corresponding author. Email: moura@ufscar.br (A.F.d.M.); kotov@umich.edu (N.A.K.)

Published 9 April 2020 on *Science* First Release
DOI: 10.1126/science.aaz7949

This PDF file includes:

Other supplementary material for this manuscript includes:

Materials and Methods

Experimental Methods

Chemicals: Gold chloride trihydrate ($HAuCl_4 \cdot 3H_2O$, ≥99.9% trace metals basis), ultra-pure silver nitrate ($AgNO_3$, 99.9999% trace metals basis), copper(II) chloride dihydrate ($CuCl_2 \cdot 2H_2O$, ≥99.99% trace metals basis), *D*-cysteine hydrochloride monohydrate (≥98%), *L*-cysteine hydrochloride monohydrate (≥98%), *DL*-cysteine hydrochloride (≥95%), hexadecyltrimethylammonium bromide (CTAB, ≥99%), thioglycolic acid (TGA, ≥99%), *D*-penicillamine (98-101%), and *L*-penicillamine (99%) were all purchased from Millipore Sigma. Another form of racemic *DL*-cysteine was prepared by mixing *D*- and *L*-cysteine hydrochloride monohydrate together until no apparent CD peaks were detected in the CD spectrum.

Even though undetectable by spectroscopic means, there is always a small excess of one of the enantiomers which can be observed under special conditions of chiral amplification, which needs to be kept in mind when assuming the racemic nature of the mixtures of amino acids and other chiral compounds. It is also important to point out that the commercial *D*- and *L*-isomers of cysteine and other amino acids are not entirely identical in chemical composition due to the difference in processes for their synthesis, extraction, and purification. Consequently, admixtures present in both enantiomers differ not only in chirality but also in chemical structure.

Synthesis of HOPs and nanoparticle assemblies: *Solution A:* CTAB (8.23 mmol, 3.0 g) was dissolved in 25 mL DI water and gold chloride trihydrate (0.51 mmol, 200 mg) was dissolved in 5 mL DI water. The CTAB solution was then mixed with the gold chloride solution, leading to the formation of a brown dispersion with precipitates. Incubating this dispersion at 70 ^{o}C for 12 h resulted in a complete dissolution of the precipitates and formation of a brown transparent dispersion. Note that CTAB in the range of concentrations used in these preparations is expected to exist in spherical or cylindrical micelles. Cetyltrimethylammonium cations (CTA^+) can react with $AuCl_4^{3-}$ and form $AuCl_4^{3-} - CTA^+$ complexes of variable composition, which is insoluble in water but can be solubilized by CTAB micelles. This agrees well with our experimental observations during the preparation of ***Solution A***. Initially mixing CTAB with $HAuCl_4$ resulted in a light yellow precipitate that can be identified as an $AuCl_4$-CTA complex, which later disperses

to become a transparent solution. Reducing the concentration of CTAB leads to yellowish or brown precipitates, which cannot be completely solubilized even at 70 °C for 12 h.

Solution B: Silver nitrate (0.029 mol/L, 5 mg/mL) or copper chloride (0.029 mol/L, 5 mg/mL) aqueous solution. Details are as follows: $AgNO_3$ (0.29 mmol, 50 mg) or $CuCl_2 \cdot 2H_2O$ (0.29 mmol, 50 mg) was first weighed out and put into a 20 mL vial. Then 10 mL deionized water was added to completely dissolve the salt at 20 °C.

Solution C: *D*-, *L*-, or *DL*-cysteine (0.57 mol/L, 100 mg/mL) aqueous solution. Details are as follows: *D*-, *L*-, or *DL*-cysteine hydrochloride monohydrate (1.14 mmol, 200 mg) was first weighed out and put into a 5 mL vial. Then 2 mL deionized water was added to totally dissolve the salt at 20 °C.

Solution D: cysteine (0.57 mol/L, 100 mg/mL) aqueous solution with different χ values (*e.g.*, ±100, ±98, ±96, ±94, ±92, ±90, ±88, ±86, ±84, ±82, ±80, ±60, ±30, 0 %). The χ values were determined by the following equation:

$$\chi = \left[\left(\frac{L - D}{L + D}\right) \times 100\right] \%$$

where *L* and *D* are the moles of *L*-cysteine and *D*-cysteine, respectively. The cysteine solutions with different χ values were obtained by mixing a 0.57 mol/L pure *D*-cysteine aqueous solution with a 0.57 mol/L pure *L*-cysteine aqueous solution with different volume ratios. For example, 900 μL *L*-cysteine solution mixed with 100 μL *D*-cysteine solution resulted in a cysteine solution with $\chi = +80\%$.

Solution E: *D*-, *L*-penicillamine (0.57 mol/L, 85 mg/mL) or thioglycolic acid (0.57 mol/L, 52.5 mg/mL) aqueous solution. Details are as follows: *D*-, *L*-penicillamine (1.14 mmol, 170 mg), or TGA (1.14 mmol, 105 mg) was first weighed out and put into a 5 mL vial. Then 2 mL deionized water was added to totally dissolve them at 20 °C.

Solutions B, ***C, D*** and ***E*** were freshly prepared before use for every experiment to avoid oxidation.

Racemic samples of cysteine were obtained by two methods: one was purchased from Sigma and one was prepared in-house by mixing equal amounts of enantiopure components purchased from the same company. The commercial product from Sigma displayed some chiroptical activity. In all cases when *DL*-cysteine is referred to in this study, the in-house-prepared racemic mixture was used unless otherwise stated. This sample was tested for near-zero chiroptical activity in all instances.

Synthesis of Au-Cys HOPs and related complex particles: In a typical experiment, ***Solution A*** was firstly cooled down from 70 °C to 40 °C, and then 200 μL of ***Solution C*** was added to 1 mL of ***Solution A***. In the experiments to study the phase diagrams and role of different parameters controlling the self-assembly pathways, 1 mL ***Solution A*** was kept at isothermal conditions at different initial building block nucleation temperatures, t_n, (*e.g.*, 20, 25, 30, 35, 40, 45, 50, 55, 60, 65, 70 °C), and then mixed with 200 μL of ***solution D*** with different χ values (*e.g.*, ±100, ±98, ±96, ±94, ±92, ±90, ±88, ±86, ±84, ±82, ±80, ±60, ±30, 0 %). After shaking for 1.5 min, the mixture was kept at t_a = 70 °C to assemble for 5 hours to provide analogous conditions for the assembly of all types of building blocks. The volume of ***Solution C*** or ***Solution D*** was small compared to the volume of ***Solution A***. As regards the concentrations of each reagent, there is a 5.7-fold excess of cysteine with respect to gold ions. White precipitates formed at the bottom of the dispersions. After the reaction was finished, the upper transparent part of the dispersion was removed by a syringe. The bottom precipitates were washed with DI water three times, to remove excess CTAB and cysteine, *etc.*, which results in easy dispersion of precipitated particles.

Synthesis of Au-Pen CLIPs and Au-TGA and related complex particles: The preparation of supraparticles with ligands penicillamine or TGA followed the same procedure as the preparation of Au-Cys CLIPs. In a typical experiment, ***Solution A*** was firstly cooled down from 70 °C to t_n = 40 °C, and then 200 μL of ***Solution E*** was added to 1 mL of ***Solution A***. After shaking for 1.5 min, the mixture was kept at t_a =70 °C to react for 5 hours. After the reaction was finished, the upper transparent solution was removed by a syringe. The bottom precipitates were washed with DI water three times to remove excess CTAB and ligands, *etc.*

Synthesis of Au/Cu-Cys HOPs or Au/Ag-Cys twisted ribbons: In a typical experiment, ***Solution A*** was firstly cooled down from 70 °C to t_n = 40 °C. Then, 100 μL of ***Solution B*** was added to 1 mL of ***Solution A***. Then 200 μL of ***Solution C*** was added. To investigate the effect of Ag or Cys concentrations, different volumes of ***Solution B*** or ***Solution C*** were added. After being thoroughly mixed for 1.5 min, the mixture was incubated at t_a = 70 °C to react for 2 hours. No difference in physical appearance of the dispersion was observed when the reaction was extended to 5 h. It is notable that the precipitates of Au/Ag-Cys twisted ribbons, especially Au/Cu-Cys

HOPs, settled at the bottom faster than those of Au-Cys CLIPs. After the reaction, the products were purified by washing with DI water analogous to the Au-Cys samples.

Sonication-induced disassembly: Sonication was carried out by using a 750 Watt Ultrasonic Processor (Cole-Parmer, amplitude 30%) in an ice bath (pause every second). For SEM experiments, in order to see the structures of the inner part of CLIPs, 1 min sonication was applied. For CPLE inversion, 15 min sonication was applied to break most of the secondary helicities.

Characterization: Circular dichroism (CD) spectra were obtained with a JASCO J-815 or JASCO J-1700 CD spectrometer. The CD spectra should be regarded as arising from a combination of electronic absorption between quantum states, light scattering and classical electromagnetic absorption. The circularly polarized light emission (CPLE) spectrum referred to herein is the spectrum of light flux comprising photons originating both from luminescence and scattering from the dispersion of HOPs and related NP assemblies. CPLE spectra were obtained with a JASCO CPL-300 spectrometer. CPLE spectra are independent of excitation wavelengths in terms of sign, position and shape. 350 nm monochromated light was used to obtain both PL and CPLE spectra. PL and UV-vis spectra were recorded on a FluoroMax-3 fluorometer and Agilent 8453 UV-visible spectrophotometer, respectively.

Confocal images (Fig. 1 J to M, fig. S14 A and B) were captured on a Nikon A-1 Spectral Confocal Microscope by using a customized laser wavelength (400 nm) and a collection window (550-720 nm). Other part of the confocal images (fig. S18 D and E), corresponding to the combined time-resolved fluorescence imaging and spectroscopy, were obtained on a Zeiss LSM-780 laser scanning confocal microscope with additional TCSPC (time-correlated single-photon counting) equipment from PicoQuant (PicoHarp 300, and LSM upgrade kit), using a 405 nm short-pulsed (100 ps FWHM) diode laser at a repetition rate of 50 MHz. The TCSPC fast (4 ps) electronics registers the time-of-arrival of each photon relative to the pulsed-laser trigger signal (see Figure S18 A), with a time resolution of 16 ps (time bins). The photon-counting detector was a SPAD module, by MPD, and a spectral band-pass filter (Thorlabs, FB650-40) centered at 650 nm (with 40 nm FWHM) was added in front of the SPAD module, for the lifetime measurements. The Zeiss microscope has built-in 32 spectral channels, with PMT photo-detectors, and allows routing the

light collected by the objective lens to two different ports to perform either spectrally-resolved fluorescence images (each pixel has its spectrum) or fluorescence lifetime images (FLIM), independently.

For the time-resolved spectroscopy and imaging, the procedure was to collect data combining time- and spectrally-resolved information under the same lighting (excitation) conditions to measure the time-arrival of the photons creating these images. To that purpose, after the confocal fluorescence image was obtained and the region of interest selected, the imaging method was switched to the time-resolved mode, while still using the same light path to and from the sample (except for the routing that happens after the light of the sample is collected by the microscope objective, redirecting it to the single-photon counting modules). Combining the information of both imaging methods allow precise mapping of each pixel in the FLIM image to the corresponding pixel in the spectral fluoresce image, while still distinguishing between direct light-scattering processes from those involving excited states, for every region of interest in the sample, provided that the lifetime is long enough. Data shown in Figure S18 A and B are histograms built from all photons collected in the corresponding FLIM images, while panel of Figure S18 C combines the spectral information of all pixels in panels D and E.

Scanning electron microscope (SEM) studies were carried out on FEI Helios with an accelerating voltage of 1.5 kV (landing energy 500 V, stage bias 1000 V). Transmission electron microscopy (TEM) images were obtained with a JEOL 2010F analytical electron microscope. X-ray photoelectron spectra (XPS) were obtained on a Kratos Analytical Axis Ultra apparatus. Samples and references were all cast on glass slides.

X-ray diffraction (XRD) patterns were recorded on a Rigaku Ultima IV X-ray Diffractometer using a continuous scanning mode with a scan step of 0.02 and a scan rate of 10 s per step. Small Angle X-ray scattering (SAXS) patterns were collected using a Pilatus 1M detector on a Xeuss 2.0 system (Xenocs). The duration of each acquisition was set to 1000 seconds and the beam energy was set to 8 keV (copper anode). The *q*-range was calibrated against silver behenate standard. The total reported *q*-range was achieved by combining measurements at two different sample-to-detector distances, 350 mm and 1200 mm. The two-dimensional raw images were subjected to azimuthal

integration by using Foxtrot, a freely-available software. The sample was prepared by drop casting a dispersion of Au-cysteine plates on a carbon-coated TEM copper grid (300 mesh, EMS, 10 uL of the dispersion were deposited three times, 30 uL) followed by drying under vacuum. The grids were then mounted on a 15-hole array holder (Xenocs), and the measurement took place under vacuum to reduce scattering from air. The SAXS patterns in dispersions were obtained in the capillary cells after concentrating them 10 fold by centrifugation. The scattering curve was fit with a two-parameter fit for a flat cylinder, with radius R and the thickness H.

Purified superstructure dispersions were used directly for recording CD, CPLE, PL and UV-vis spectra, and observation under confocal microscopy. SEM, TEM, XPS, *etc.* samples were prepared by drying the dispersions on silicon wafers or TEM copper grids. Powder samples for XRD, TGA were prepared by freeze-drying the HOP dispersions. The powder samples were also used in the time-resolved spectroscopy and imaging (FLIM), after properly rehydrating it with deionized water.

Statistical analysis: The average size of Au-Cys NPs was determined by the statistical analysis of diameters of 540 nanoplatelets from TEM images. The average size and other geometrical parameters of the CLIPs were determined by analyzing 500 particles in SEM images. The polydispersity indices (PDI) were calculated to be 1.36 and 1.02 for NPs and CLIPs, respectively, using the following equations:

$$D_n = \frac{\sum d_i}{n} \qquad (1)$$

$$D_w = \frac{\sum (d_i)^4}{\sum (d_i)^3} \qquad (2)$$

$$\mathrm{PDI} = \frac{D_w}{D_n} \qquad (3),$$

where D_n represents the number-average diameter and D_w represents weight-average diameter; d_i is the diameter of NPs or CLIPs measured from TEM or SEM images and n is the number of the particles. TEM and SEM images of nanoplatelets or CLIPs were randomly selected for all statistical analyses.

Computational Methods

Atomistic molecular dynamics computational models for Au-Cys structures with nanoscale dimensions: Although the DFT calculations were computationally efficient, they were nonetheless too demanding for systems larger than a few unit cells periodically replicated, so we also tested atomistic molecular dynamics (MD) methods to assess nanometer-size sections of the Au-Cys sheets. Furthermore, they were useful for the evaluation of the 3D geometry of large structures that may not have the proper helicities in periodic boundary conditions due to the damping of the chiral twisting that periodic boundary conditions enforce between periodic replicas.

An MD model of an Au-Cys zigzag gold chain was constructed, based on the structure reported by Söptei (*19*). The ratio of gold/sulfur/Cys was 1:1:1, which is consistent with the XPS spectra and all other structural data (figs. S15 to S17). Both neutral and zwitterionic Cys ligands were used in the model in accord with findings both from the PBEh-3c calculations for nonperiodic clusters and from the BP86/DZVP-MOLOPT-GTH calculations for periodically replicated unit cells.

In conjunction with MD simulations, further DFT calculations were performed with the DMol program of Materials Studio (Dassault Systems) where the generalized gradient approximation (GGA) with a Perdew-Wang (PW91) functional and an all-electron relativistic double numerical basis set augmented with a polarization P-function (DNP) was utilized. For geometry optimization, the convergence in energy and gradient was set to 10^{-5} eV and 5 x 10^{-2} eV $Å^{-1}$. The *k*-points sampling of the Brillouin zone in the geometric optimization and properties investigations were performed with the set of 6×6×1 on the basis of the Monkhorst–Pack algorithm.

MD simulations using a classical force field were used to model nanosheets comprising 512 Au atoms and the same number of cysteine surface ligands, which were either *L*-Cys or *D*-Cys. The MD simulations were performed with the Forcite Plus module in the Materials Studio suite, using the universal force field (UFF) to treat bonding and nonbonding interactions in the models. An implicit solvation model was used for all the simulations, where the relative dielectric constant of the solvent was set to 78.54 to represent aqueous phenomena. The Coulombic force was calculated atom-based with a distance cutoff of 1.55 nm. NVT ensemble was used at the ambient temperature of 298K, controlled by the Nosé method. A time step of 1 fs was employed while the total production time was set up to 10 ns before 1 ns pre-equilibrium.

Calculation of optical properties: In order to calculate the UV-vis absorption and CD spectra of the gold-cysteinate, the simplified time-dependent density functional theory (sTDA) proposed by Grimme was employed as implemented in the Orca program, using the Tamm-Dancoff approximation with an energy cutoff of 10 eV. The sTDA calculations were performed after an unrestricted ground state calculation using the long-range corrected CAM-B3LYP hybrid functional and the def2-TZVP triple-ζ basis set. The self-consistent field was calculated using the very tight convergence criteria of Orca to ensure a properly relaxed set of Kohn-Sham orbitals for the sTDA calculations. This combination of energy window and basis set size yielded a very large number of excited states for each system.

The calculations of the optical spectra for larger Au-Cys nanosheet models can be potentially accomplished by models with periodic boundary conditions. However, they provide an intrinsically poor description of the chiral shapes with long-range twists being removed between each unit cell because the periodic boundary conditions forcefully damp any twist. On the other hand, classical MD simulations can capture the tendency of the systems to form twisted structures well, but they are obviously far too large to allow any successful quantum mechanical calculation of the UV-vis and CD spectra.

The compromise was met for models that display a reasonably large size for the twist to evolve but, at the same time, could be calculated by combining the extended tight-binding (xTB) semi-empirical DFT approach along with the simplified Tamm-Dancoff approximation (sTDA)(*22*) capable of computing the electronic excitations in a 7 eV energy window needed for CLIP fragments (**Figure 2**).

The sheets were allowed to relax using the GFN1-xTB formalism as implemented in the xTB program until the energy gradient was below 2×10^{-4} E_h/bohr and the energy change between cycles was below 1×10^{-7} E_h. Further, the convergence of energy and charge changes between SCC cycles was set to 1×10^{-6} E_h and 2×10^{-5} e, respectively, which are very tight criteria.

In order to correct the static correlation error (SCE) that arises in systems with multi-reference character, such as transition metal compounds, an electronic temperature of T = 12500 K was set to induce a Fermi smearing. Besides improving SCC convergence, this correction avoided spurious transitions in the UV-vis/CD calculations.

Free energy calculations

The free energy for the process of association between two Au-Cys sheets can only be tackled for a simplified model system, using the MARTINI force field, which fuses lighter atoms into a single heavier coarse grained (CG) site. Being a heavy atom on its own, each gold atom was treated as a positively charged CG site, while each zwitterionic cysteine molecule was treated as an irregular tetrahedron with vertices corresponding to S^-, CH_2CH, NH_3^+ and COO^- groups, which were named as S, H, N and O respectively, along with Au sites for gold (Table S1). The Lennard-Jones 12-6 interaction potential was employed (Table S1), with σ and ε parameters scaled either up or down with respect to standard MARTINI force field parameter to achieve the typical geometric and energetic patterns observed for the DFT and the atomistic MD models of Au-Cys nanosheets. The non-bonding interactions were truncated at a cutoff radius of 1.2 nm along with a shift potential to take the potential smoothly to zero at the cutoff. The Coulomb interactions were scaled down by a relative dielectric constant $\varepsilon_r = 15$ to compensate the lack of dipole moment in the CG-MD water model.

Harmonic potentials were employed for constraining bonds and angles between the sites comprising the tetrahedral molecules at the equilibrium geometry (Table S2). Force constants of 8000 kJ mol^{-1} nm^{-2} were employed for the bonds and of 500 kJ mol^{-1} rad^{-2} for the angles. A further harmonic potential was assigned to the S-H-O-N dihedral angle in order to prevent chirality inversion during the simulations, with a force constant of 1500 kJ mol^{-1} rad^{-2} keeping these atoms at ±46.94º for *D*- and *L*-cysteine, respectively.

Table S1. Lennard-Jones parameters employed in the CG simulations.

Site 1	Site 2	σ (nm)	ε (kJ/mol)
S	S	0.460	4.5
S	O	0.470	4.5
S	N	0.282	4.5
S	H	0.282	3.5
S	Au	0.230	40.0
O	O	0.470	4.0
O	N	0.282	5.0
O	H	0.282	3.5
O	Au	0.470	4.5
N	N	0.282	3.5
N	H	0.282	2.7
N	Au	0.282	4.0

H	H	0.282	3.1
H	Au	0.282	3.5
Au	Au	0.460	5.0

Table S2. Equilibrium bond lengths and angles for the CG Cys molecule.

Bond	Length (nm)	Angle	Value (degree)
S - O	0.377	N - H – O	69.790
S - N	0.410	N - H – S	66.100
S - H	0.288	N - O – S	43.212
O - N	0.239	H - O – S	45.257
O - H	0.221		
N - H	0.213		

The model Au-*L*-Cys nanosheets were drawn in agreement with the detailed models derived using DFT and atomistic MD simulations, with an inner bilayer of 512 Au atoms in a zigzag arrangement, with one zwitterionic *L*-Cys molecule *per* Au atom (Fig. S5). The rectangular models had their lengthier direction either in the [100] or the [010] crystallographic directions.

Before performing the actual free energy calculations, these structures were optimized using the steepest descent algorithm as implemented in the GROMACS package v2018.4. We initially set the Au charge to 2+ and the S charge to 2- to induce an orderly crystalline arrangement, followed by an NPT molecular dynamics using anisotropic pressure coupling at 1 bar, 362 K and periodic boundary conditions in the sheet plane, with vacuum below/above the system. During the whole optimization process, we observed extensive shearing of Au atoms to form hexagonal patterns similar to those observed in the models with atomic details. The steepest descent optimization and the MD simulation were repeated with the correct charges, without any appreciable structural or energetic change.

Experimentally, homochiral sheets formed stable twisted structures, so we performed the scan of the twisting angle for the sheets with *L*-Cys and cutting directions [100] and [010]. At each step of the scan the structures were partially optimized, freezing the coordinates for the Au and S sites and relaxing the remaining sites by the steepest descent algorithm until forces converged to values below 25 kJ mol^{-1} nm^{-1}, followed by another round of energy minimization with the conjugate gradient algorithm until forces converged to values below 15 kJ mol^{-1} nm^{-1}. Each sheet was placed in a 50 nm x 50 nm x 50 nm box to avoid interactions with their periodic images. Electrostatic

interactions after the cutoff distance of 1.2 nm were treated by means of a particle-mesh Ewald summation. The Lennard-Jones interactions were calculated up to 0.9 nm and a switching function was used to bring them to zero at 1.2 nm.

The phase space corresponding to the association of both Au-*L*-Cys sheets was sampled using our lab-made software *Themis*. As discussed elsewhere, it performs a combination of translation, rotation and gyration movements of one structure around a reference structure using grids to discretize the configurational phase space. In principle, a full scan should be done for all relative orientations and distances between the two sheets, but we used the experimental information that sheets grow in the *ab* crystallographic plane and for aggregates in the *c* direction to narrow the search only close to these growth or stacking directions, which we named as head-to-tail and face-to-face directions.

We considered the lowest energy structure obtained after the twisting scan for each sheet, with the reference sheet centered at (0,0,0) with the longer axis in the *y* direction. The translation grid for the face-to-face interactions was done along the *z*-axis in the range between 1.50 nm and 1.80 nm, in 0.02 nm intervals, while the head-to-tail interactions were done along the *y*-axis in the range between 7.80 nm and 7.95 nm, in 0.01 nm intervals (these distances refer to the reference sites placed at the center of the face and the center of edge of the sheets, respectively). Further rotations performed around the *z*-axis were also considered to improve the phase space sampling, yielding 2880 different structures for the face-to-face interactions and 160 structures for the head-to-tail interactions.

Interaction energy between the two sheets was calculated for every configuration using the MARTINI potential (Table S2), as implemented in labmade *Themis* software. For each system, the partition function was calculated considering the interaction energy *per* Au-*L*-Cys unit cell. This normalization of the total interaction energy per structural unit is necessary to turn the otherwise extensive thermodynamic properties into their intensive counterparts.

Electrodynamic computations

The CD spectra of CLIPs in the long wavelength range ($\lambda > 500$ nm) were calculated using a commercial FDTD software, Lumerical FDTD solutions. The CLIP was modeled with six twisted nanoribbons aligned in both the positive and the negative directions on the three Cartesian coordinate axes. Each twisted nanoribbon approximates effective chirality projected onto each of

the coordinate axes. This enabled us to simplify the CLIP model from chirality in spherical coordinates to Cartesian coordinates.

A model twisted nanoribbon that comprises the CLIPs was constructed with computer-aided design software, whose geometrical features are as follows: l = 1300 nm in length, w = 150 nm in width, t_h = 64 nm in thickness. The six nanoribbons were placed onto a sphere (r = 450 nm) that was aligned in the three Cartesian coordinate axes.

Two CLIPs, Au-*L*-Cys and Au-*D*-Cys, were modeled with right-handed and left-handed twists projected in the twisted ribbons, respectively. The refractive index of the gold-cysteinate was calculated from DFT simulations. The CD spectra were obtained by the difference between the extinction cross-section subjected to the left-handed and the right-handed circularly-polarized input light.

Graph Theory Methods

The complexity of structures assembled from nanoscale components was enumerated in this work by utilizing methods of graph theory (GT). The inspiration for this research effort was the fact that a variety of molecular and condensed phase properties from UV-vis peaks to phase transitions can be correlated with GT indexes developed in the framework of organic and inorganic chemistry. Since the mathematical toolbox of GT is scale-free, we hypothesized that GT can also be utilized to describe the structure and to eventually establish structure-property relationships for the nanoassemblies.

Similarly to the discretization of molecules into atoms, we first discretized nanoassemblies into simple nanoscale building blocks (for example, nanoparticles, nanoplatelets, nanoclusters, *etc*). The centers of mass of the nanoscale building blocks serve as nodes. The nanoscale particles often undergo the process of nearly epitaxial merger of the crystal lattices. When this and similar processes take place, resulting in lattice-to-lattice connectivity of the nanoscale elements of nanoassemblies, and when the building blocks of assemblies have a more complex geometry than the basic elements (*i.e.* nanoparticles, nanoplatelets, nanoclusters), these elements will be represented as graphs themselves.

The nanoscale building blocks that we consider in this study are nanoplatelets and nanospheres based on gold sulfide. They are inorganic, whereas the interfaces between them in nanoassemblies are created by organic molecules (*e.g.* Cys, TGA, and Pen). The same is true for a vast majority

of other nanoassemblies. The supramolecular linkages formed by the layers of these organic ligands *following non-random pattern* will be denoted as edges. If the nodes share organic interfaces, they are connected with an edge. The number of edges converging onto one node cannot be infinite, because it will be un-physical to have infinite number of linkages made by one building block. If there is no connecting material between them, the nodes remain disconnected.

Following these discretization rules, the structural multigraphs of self-assembled structures from nanoscale components – they will be referred here for brevity as GT-models – can be constructed for a wide range of experimentally observed 3D architectures self-assembled from a variety of materials. When nanoscale components assemble into semi-infinite structures such as chains, sheets, ribbons, *etc.*, the GT-models are constructed with an identical approach. To be consistent with the discretization methods outlined above, semi-infinite structures that underwent oriented attachment will be represented as minimal topological contracts (MTCs) that are defined as finite graph segments retaining the essential aspects of 3D geometry of the semi-infinite assemblies. For instance, a straight chain of NPs that have fully merged inorganic lattices or a nanowire (fig. S26a) will be represented as two nodes connected with an edge, also known as a K_2 graph because a minimum of two points is needed to define a straight line (fig. S26b).The MTC of a single crystalline sheet of mesoscale dimensions formed by assembly of the nanoscale building blocks is K_3 because a minimum of three points are needed to define a plane (fig. S26, c and d). Twisted sheets and ribbons will be represented by the pentagonal Kuratowski K_5 graph to account for their twisted shape, because the K_5 graph is the minimal representation of 3D chiral structures (fig. S26, e and f) (*32*).

Infinite and semi-infinite periodic structures can also be reduced to finite GT-models known as quotient graphs, which reflect the variety of translationally equivalent nodes in the periodic structures. In this study, we shall use the MTCs because the quotient graphs of semi-infinite helical structures have different numbers of translationally equivalent nodes depending on the pitch. This problem makes them unsuitable for consistent assessment of complexity when assemblies have identical geometry but different pitches.

An important case of nanoassemblies is the one that would have no or dynamically variable short-range (local) bonding pattern between the nanocomponents, but they would have long-range organization pattern. Such nanoassemblies are exemplified by phase-separated nanoscale components, dynamic assemblies (flocks, swarms, …), supraparticles, and hierarchical

assemblies. Their GT-model will be a cyclic graph encircling the area where nanoscale components are located (phase separated) with a subgraph inside the circle depicting the MTCs of the present nanocomponents. Note that the number of nanocomponents in these long-range assemblies can be multiple, which will certainly increase their complexity. A simple example of such graph is a loop with one node and one edge with unconnected nodes inside that representing individual randomly positioned nanoparticles (fig. S26, i and j). This particular GT-model describes a supraparticle that has no specific local organization between constituent nanoparticles at nanoscale. At the same time, the nanoparticles forming supraparticles are not randomly distributed and their formation is associated with substantially reduced entropy of the system that is represented by the surrounding loop.

Multiple GT indexes and functions (*e.g.* generalized fractal dimension) can be calculated from graphs characterizing nanoscale assemblies. Here we use the complexity index, *CI*, calculated as a modified augmented valence complexity (AVC) algorithm based on augmented valence of an individual nodes (AVV) that was used by Randic and Plavsic to describe the complexity of organic molecules (*33*). The key reason for using *CI* is that it enables the enumeration of structural complexity based on connectivity patterns of nodes. Also important, *CI* can be calculated for multigraphs, *i.e.* graphs that contain loops, and for graphs with small number of nodes representing, for instance supraparticles and similar phase separated nanoscale systems, which would be difficult for generalized fractal dimension function and other GT functions enumerating complexity more suitable. Furthermore, *CI* and AVC with modifications described below is also applicable for the description of complex infinite assemblies with large number of nodes. Last but not the least, the *CI* is computationally straightforward and yields finite quantities even when graphs are infinite. These mathematical aspects make *CI* values applicable to a variety of nanoscale assemblies.

The value of *CI* of a particular graph represents the amount of non-random and non-repetitive information that is contained within the GT-model. To have some numerical sense of *CI*, its value for a single node is zero, $CI = 0$. If there is any number of randomly distributed single nodes in a given volume, *CI* will remain zero. The value of *CI* for K_2, K_3, and K_5 representing self-assembled monocrystalline straight nanowire, flat nanosheet, and twisted nanoribbon, is 1.5, 4.0 and 12.0.

Consistent with GT algebra, the *CI* for GT-models including loops describing, for instance supraparticles with no short range order, are calculated as the sum of the *CI* of the two subgraphs:

one is the loop with nodes and edges connected to it and the one inside the loop representing the elementary building block of the supraparticle.

Consistent with the discretization methods described above and with the fact that for randomly distributed single nodes in a given volume *CI=0*, it does not matter how many individual nanoparticles, nanoplatelets, nanoclusters or other constituent building blocks form a supraparticles. They all can be represented by a single MTC: K_1 for nanoparticles, K_2 for nanowires, K_3 for nanosheets, *etc*. The same is obviously true for the dynamic systems when the structural blocks of the supraparticles form as a result of the merger of smaller building blocks. If there is no specific order between them, they are represented by a single MTC inside the loop. As such, *CI* of a supraparticle assembled from individual nanoparticles is 2.0 (fig. S26, i and j). When a similar assembly is made from nanoplatelets, its *CI* = 6.0 (Fig. 4, A and B, fig. S26, k and l).

Importantly, for fairly complex structures, the AVC method is calculated for all symmetrically non-equivalent vertexes as defined by non-equivalence of the mathematical form of the equations used to calculate the augmented valence sum (*33*). The *CI* of the complex structure calculated here for all particles and other structures is the sum of the augmented vertex valence for all non-equivalent vertexes. Note that summation components of *CI* rapidly decay as $1/2^N$ where *N* is the distance in edges away from the node of interest, and therefore can be easily applied to and calculated for infinite and semi-infinite structures since these infinite sums converge.

Our modification of AVC for HOPs and other nanoassemblies included nearest-neighbors approximation (NNA) introduced for consistent calculation of *CI* values when the structures become large, but have repetitive motifs that do not increase information content of the graph. In classical AVC, all nodes are grouped into classes of symmetrically equivalent nodes, *i.e.* the nodes with exactly the same sequence of edges stemming from the node. (Note that the notion of being 'symmetrical equivalence' in GT is different than in the traditional geometry). All symmetrically equivalent classes of nodes must be included in the summation process. Importantly, the nodes belonging to the one equivalence class must be only once per class, thus resulting in leading to *CI =AVC= AVV(class 1) + AVV(class 2) + AVV(class3).* The summation of AVVs from different classes of nodes rather than from different nodes reduces the contribution to AVC from repetitive structures that in this formalism do not increase complexity.

Many nanoassemblies and HOPs are represented by semi-infinite GT-models with repeating structures, such as sequence of spikes or sheets (Table 3). In this case, the direct

application of AVC would result in infinite complexity, which is certainly inadequate. For example, a semi-infinite array of spikes or sheets located on one side of particle with a phase boundary (figS10B, also Table 3) will result in an infinite number of unique nodes and thus unphysically large *CI*. NNA addresses this issue. NNA postulates that the nodes belong to the same equivalency class (and thus counted only once) when they have equivalent first nearest-neighbors. By other words, if the nodes located one edge away from each other have identical graph describing their surrounding with one edge limit, they are declared symmetrically identical. In the case that NNA is applied, the contribution to *CI* from that equivalence class is calculated using the node within the semi-infinite structure, rather than a node near the boundary.

For example, the GT model of irregular nanostar with metallic nanospikes is composed of a semi-infinite array of K_2 MTCs on a loop **(Table S3**). With or without the NNA, there are only two symmetrically unique nodes in these array of spikes - the node at the base of a spike, and a node at the end of a spike. At the same time, when the same array of spikes is grown on a particle from different materials as in Janus nanostar, the phase boundary needs to be reflected in the GT model that results in the second loop and a node. Without NNA, half of the nodes representing the spikes would be unique due to the existence of this additional node of the second phase. This would result in inconsistently high *CI* (infinite) compared to the irregular nanostar. When one applies NNA, the summation is reduced to just four classes of symmetrically equivalent nodes. The nodes at the base of spikes are able to be reduced to be either a node within the spike array, or a node that neighbors the phase boundary; all nodes at the tips of the spikes are all treated the same since each one has the same nearest neighbor(s), a single node with the degree of three; and the node at the phase boundary, which is symmetrically non-equivalent to all other nodes.

Supplementary Figures and Tables

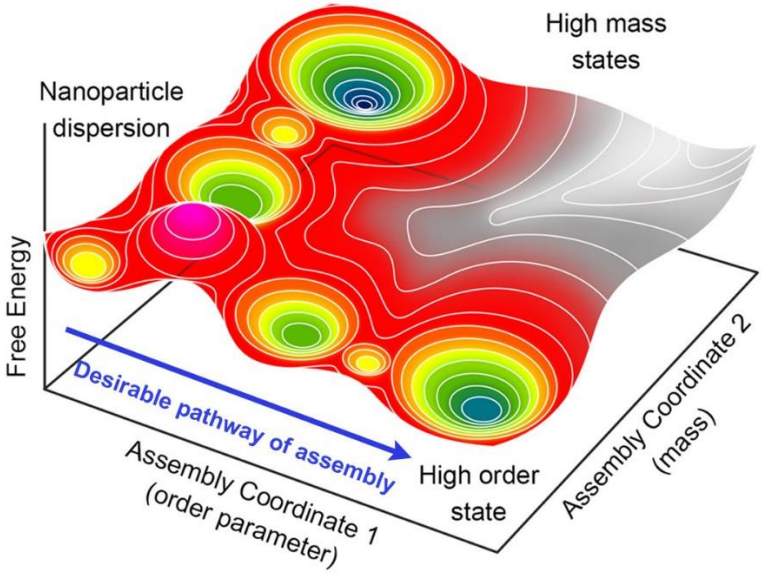

Figure S1. Schematics of the thermodynamic landscape for self-assembly of nanoparticles and other building blocks into higher order structures. Order parameters related to the structure of nanoassemblies can be exemplified by the periodicity of particles in a chain, sequence of particulate layers, size of the assemblies, crystal packing, and complexity index (*CI*) discussed below. As applied to HOPs, structural order parameters can be aspect ratio of spikes, periodicity of stacking of the nanosheets, pitch of the twisted ribbons, total number of spikes per particle, complexity indexes, *etc*. Order parameters related to their properties can be exemplified by light scattering intensity, maximum wavelength, circular dichroism intensity, colloidal stability, *g*-factor, and circularly polarized light scattering discussed below.

From the perspective of thermodynamics and interactions of particles traversing this complex free energy landscape, the difference in free energy between the two enantiomers of chiral molecules is 0.25-0.5 k_bT, which is much lower than the interaction energy between nanoparticle amounting to 3-200 k_bT. The interaction energy and structural influence of molecular chirality can potentially be enhanced via collective effects, but numerous agglomeration pathways independent of mirror asymmetries will be enhanced as well, further biasing the products toward stochastic agglomerates.

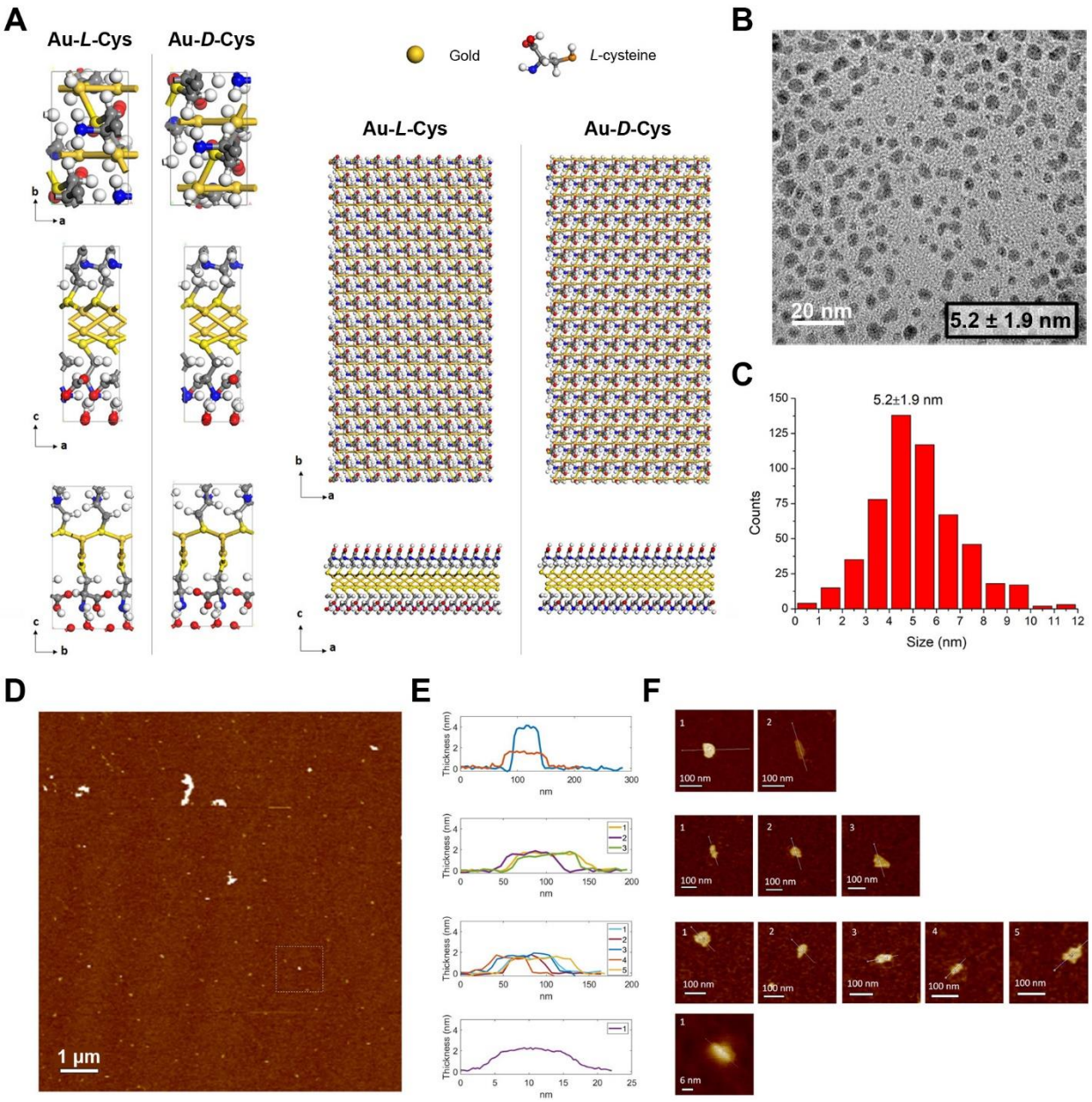

Figure S2. Molecular and nanoscale structure of Au-Cys nanoplatelets. A, Structural model of the Au-Cys unit-cell (left) and nanoribbon (right) along different crystallographic axes; thickness of the nanoribbons is 1.37 nm along c- or [001] direction based on the calculated atomic structure. **B,** TEM image of Au-Cys nanoplatelets observed in the initial stages of self-assembly of gold cysteinate particles. **C**, Statistical analysis of the size of 540 Au-Cys nanoplatelets based on *ImageJ* software analysis of TEM images. **D,** Survey AFM image taken on with numerous nanoplatelets visible in the scanned area. **E,F,** AFM line scans (E) and images (F) of individual building blocks revealing their nanoplatelet shape and formation of the short stacks. The AFM images were obtained immediately after mixing the reactants, t_n = 20 ^{0}C at $\chi = 0$. The dispersions were deposited on silicon substrates and washed with DI water.

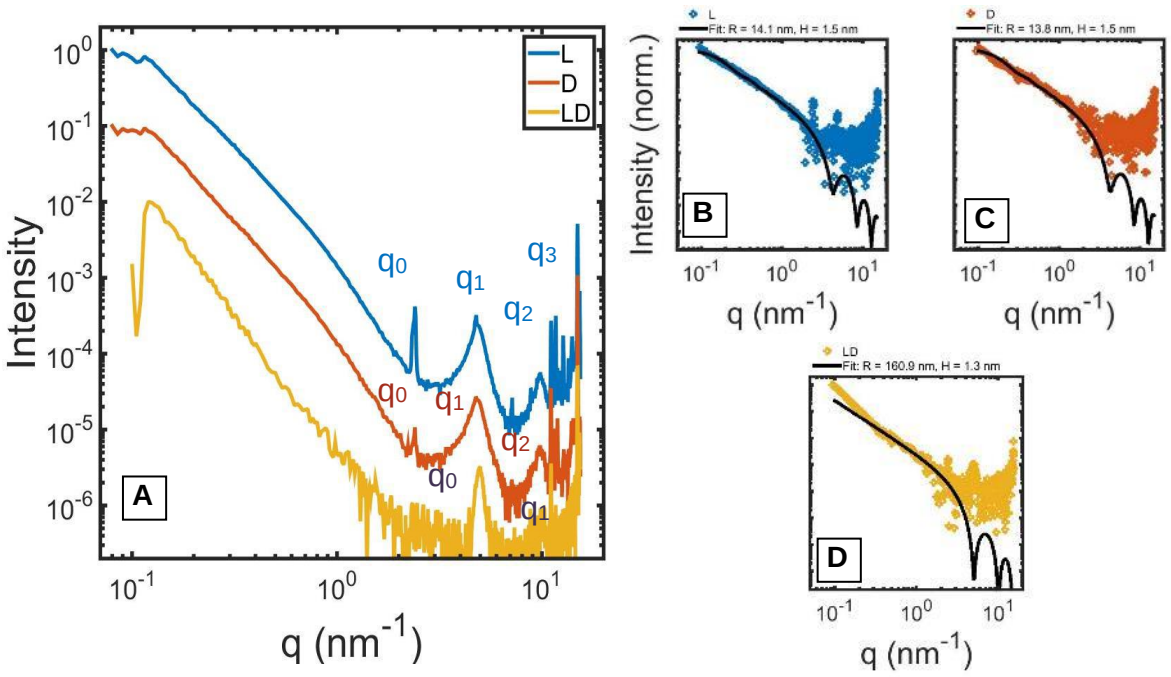

Figure S3. Small angle X-ray diffraction (SAXS) pattern obtained for the early NPs (A) deposited on TEM grid as thin films and (B to D) in dispersion. The SAXS data from the films reveal superposition of two basal spacing progressions of laminated platelets with the characteristic distances of 1.25-1.29 nm and 2.4 nm. The peaks for 1.25-1.29 nm periodicity match very well the thickness of the hydrated platelets obtained in AFM and DFT model. The characteristic distance of 2.4 nm may be attributed to stacks of tightly bound double-platelets (see S2E,F) with an offset between them resulting in basal spacings with double periodicity.

SAXS data from dispersion after concentration were fit with a two-parameter model for a flat cylinder, with radius *R* and the thickness *H*. The best fit resulted in the dimensions H = 1.5, 1.5, 1.3 and *R* = 14.1, 13.8, 160 nm for L-, D, and *rac*-platelets, respectively. Variations and increase in the lateral size for these samples was caused by the 10x concentration step to increase the signal-to-noise ratio. Based on all these results, one can firmly conclude that the early particles (*i.e.* building blocks of the assemblies) observed for $\chi = 100\%$ and $t_n = 20\ ^{o}C$ are nanoplatelets.

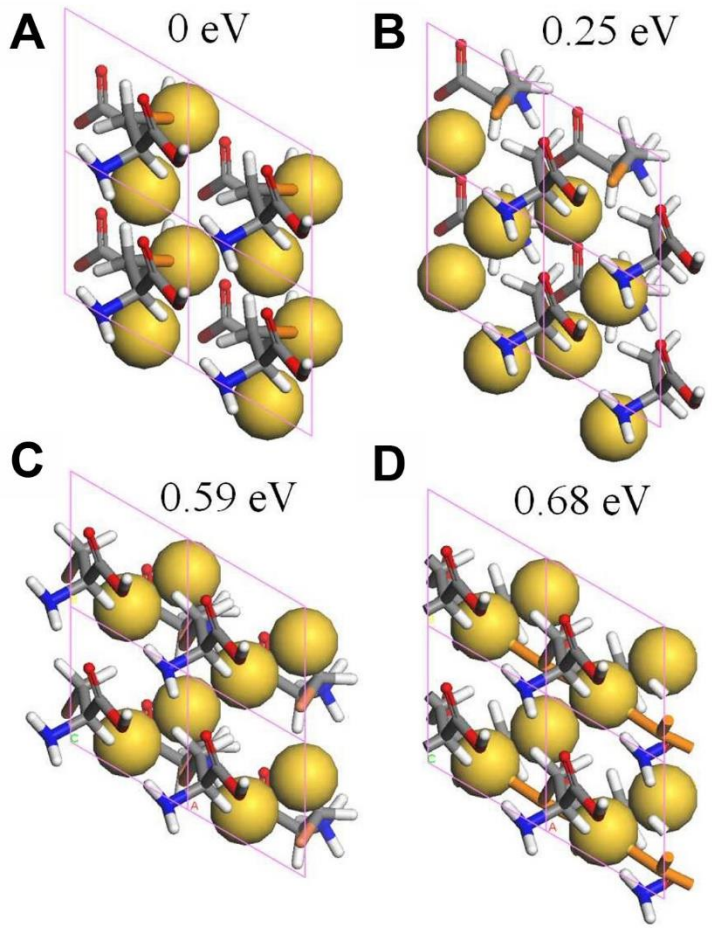

Figure S4. DFT models for four possible Au-Cys unit-cells and the corresponding relative energies. Each model has been fully structurally optimized. Model (A) reflecting [010] growth patterns nanoplatelets into nanosheets has the lowest energy. Hence, [010] unit cells served as a basis for chosen for MD simulations of Au-Cys nanosheet models. Complementary XRD (fig. S15) and other data (fig. S16) validate [010] molecular structure of the Au-Cys nanoribbons. The energies of the atomistic segments are given as relative values in respect to the structure in (A) used as a reference.

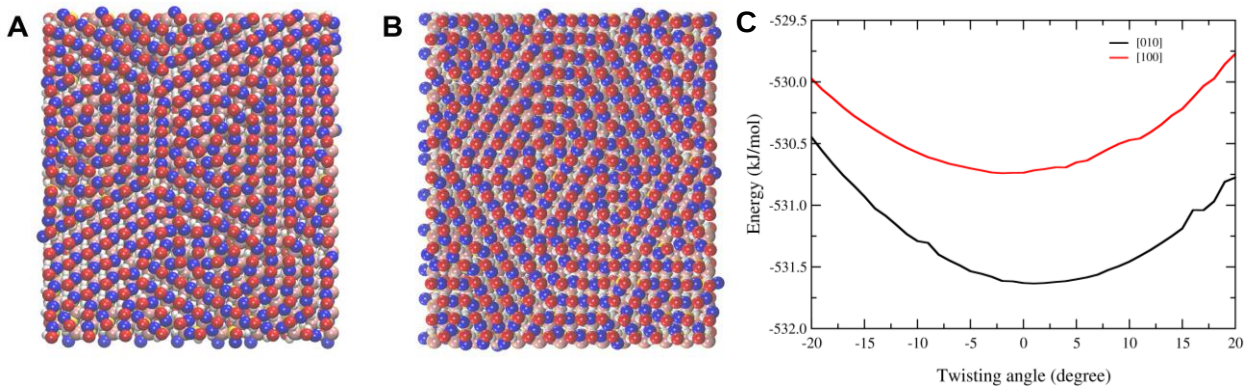

Figure S5. Coarse-grained models for the Au-*L*-Cys sheets. **A,** Preferential growth in [010] crystallographic direction. **B,** Preferential growth in [100] crystallographic direction. **C,** Total potential energy *per* $(Au\text{-}S)_2$ unit cells for the uniform torsion of the CG model sheets in (**A**) and (**B**) around their longer axis. The minimum twisting angle for [010] nanoplatelets of this size is +1 deg, which corresponds to the RH twisted nanoribbon with pitch length of 5400 nm, which can be compared with 1300 ± 123 nm observed in the experiment (**Figure 1**). Besides having lower thermodynamic stability, [100] platelets have ΔG minimum at a twist angel of -2 deg, which would result in a LH twisted ribbons contradicting the experimental observed geometry.

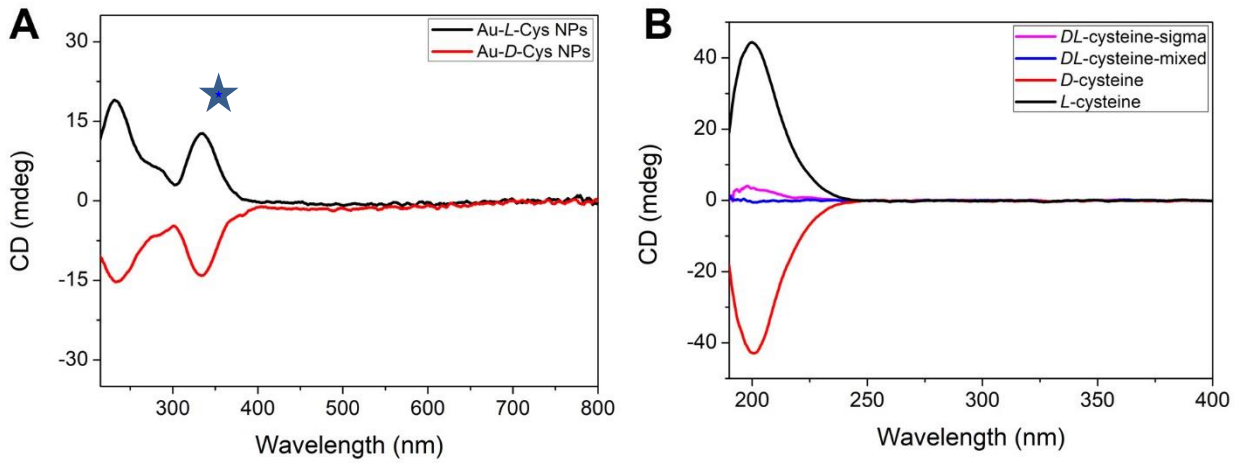

Figure S6. CD spectra of gold cysteinate (Au-Cys) nanoplatelets (A) and free Cys (B). CD spectra of Au-Cys nanoplatelets recorded immediately after mixing Cys with $HAuCl_4$/CTAB solutions. *D*-, *L*- and *DL*-cysteine solutions in (B) are 5.7 mM. Two new peaks at ~290 nm and ~340 nm appear for Au-Cys nanoplatelets compared to the spectrum of free Cys; they are associated with mirror asymmetry of excited electronic states and the twisted shape of the nanoplatelets. The peak marked by the blue star corresponds to the chirality of nanoplatelets.

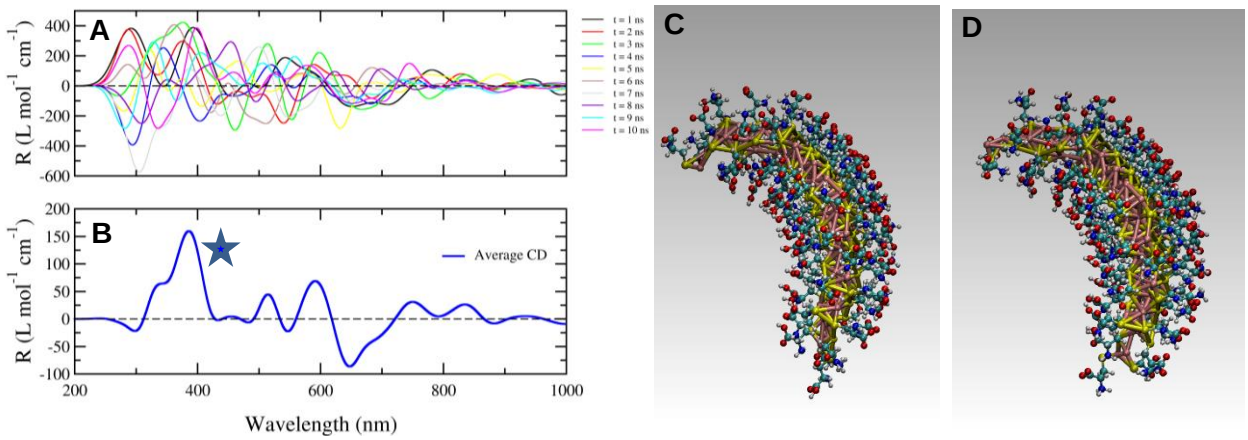

Figure S7. Calculated CD spectra for the Au-*L*-Cys nanoplatelets obtained by xTB-sTDA calculations of ten Au-*L*-Cys nanoplatelets. Rotational strength (CD) spectra obtained by xTB-sTDA calculations of (**A**) ten Au-*L*-Cys nanoplatelets with geometries taken from the UFF MD simulation over a period of 10 ns; (**B**) the average spectrum was obtained by integration of rotatory strengths for all the electronic transitions and applying Gaussian broadening with a full width at half-maximum (FWHM) of 80 nm (See also fig. S19). The flexibility of the platelets resulting in averaging of positive and negative dichroism lead to disappearance of many long-wavelength bands by mutual cancellation as compared to the spectrum with fewer bands in Fig. S6A (see also fig. S8). The prominent peak in the UV part of the spectrum (marked by a blue star) was not cancelled out by thermal agitation and as such must be considered as a fingerprint of the permanent chirality of the nanoplatelets. (**C** and **D**) The atomistic models of the nanoplatelets observed for 1 (C) and 9 (D) ns of MD simulations.

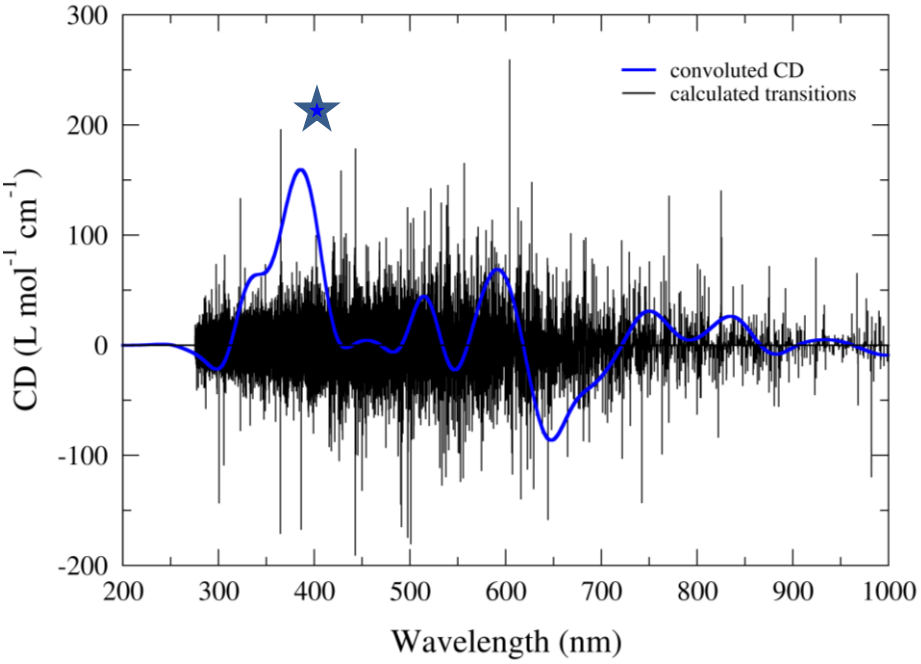

Figure S8. Integrated CD spectrum with corresponding electronic transitions. The black vertical lines depict over 75000 individual transitions for the ten spectra depicted in Fig. S7A, while the averaged blue spectrum was obtained using a Gaussian broadening with a FWHM of 80 nm. The sign of the resulting bands especially in the long wavelength part of the spectrum is the result of compensation of polarization rotation for many transitions. The band in the UV part of the spectrum is the band corresponding to the early nanoplatelets observed in experiment.

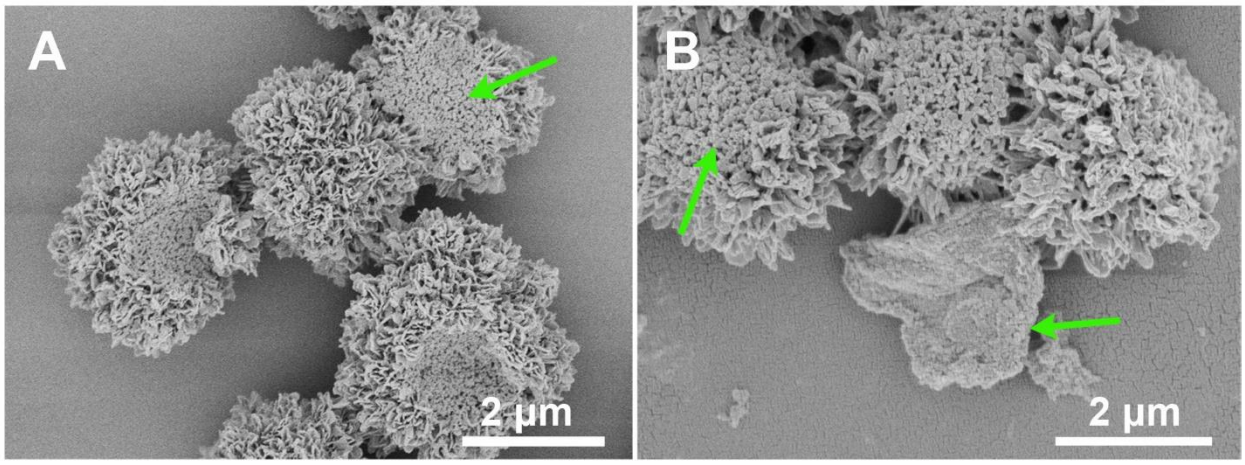

Figure S9. Example of assembly of Au-*L*-Cys nanoplatelets in sub-optimal conditions. A,B, Assembly of Au-Cys nanoplatelets with the presence of 0.5 mol/L NaCl and absence of CTAB under the same conditions as the particles assembled in **Figure 1** with t_n = 40 °C and t_a = 70 °C for 5 h. The high porosity of agglomerates is associated with the high dispersity of the nanoplatelets.

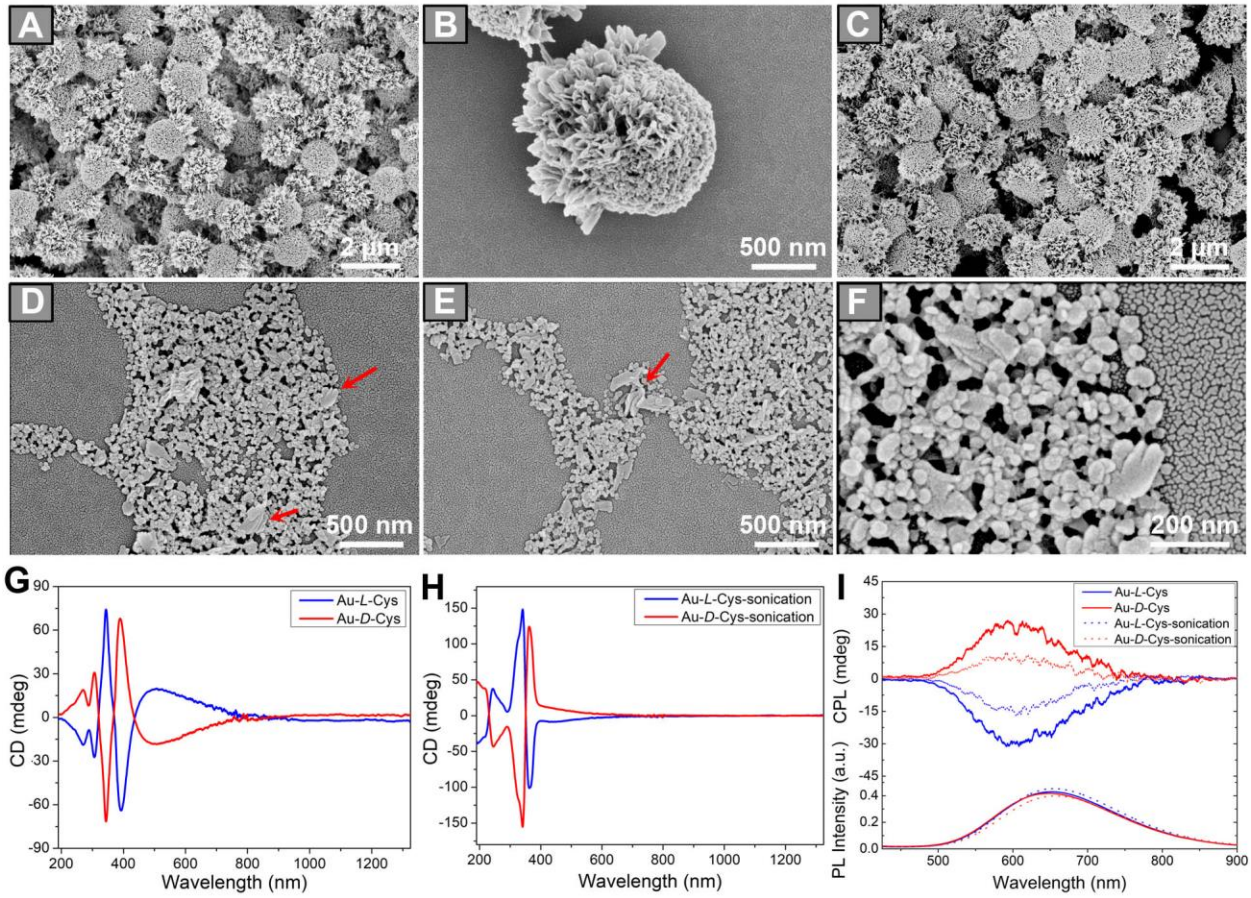

Figure S10. Au-Cys half-spiked spheroids obtained by assembly of Au-Cys nanoplatelets without CTAB. SEM images of (**A** and **B**) Au-*L*-Cys particles and (**C**) Au-*D*-Cys particles; t_n = 40 °C and t_a = 70 °C for 5h. **D** to **F,** SEM images of (D and F) Au-*L*-Cys and (E) Au-*D*-Cys after sonication for 10 min. Sonication disassembled half-spiked spheroids into constituent nanosheets. Red arrows indicate larger twisted ribbons with two levels of helicity. **G,H,** CD spectra before (G) and after (H) sonication. **I,** CPLE spectra before and after sonication. The particles in figure S10 are also fluorescent. Au-*L*-Cys dispersions showed a negative peak for the circularly polarized emission (CPLE), while Au-*D*-Cys samples showed a positive one. This indicates that in these particles, chirality at the molecular and nanoscale levels dominate the CPLE properties, as opposed to the CLIPs from **Figure 1** and **2**, whose CPLE activity is determined by scattering of the twisted spikes. The high porosity of the half-spiked spheroids is associated with the high dispersity of the nanoplatelets.

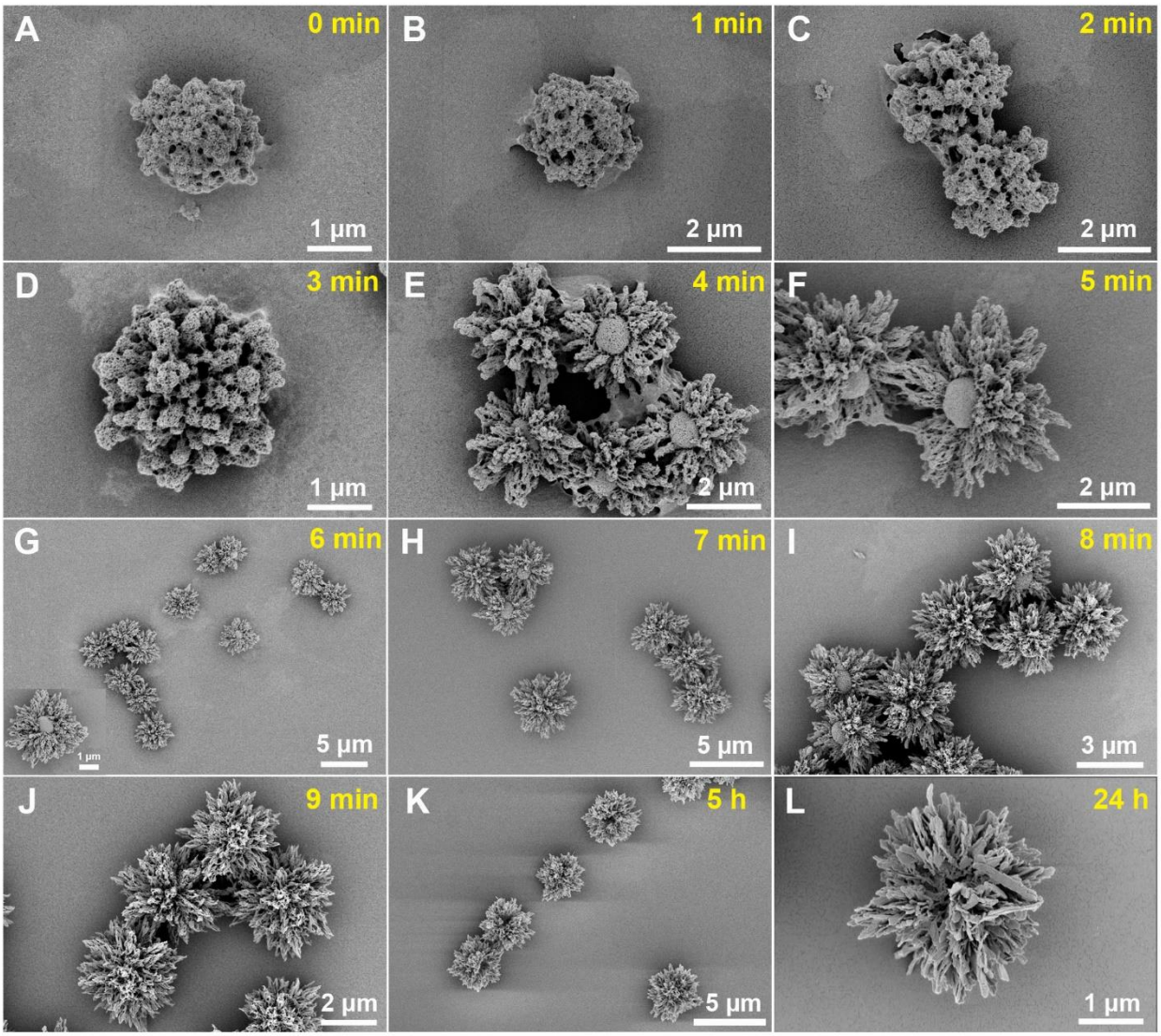

Figure S11. SEM images obtained for the growth process of Au-*L*-Cys CLIPs. The stages of the formation of CLIPs indicate complex process of nanoscale organization that starts with the formation of nearly spherical supraparticles. The formation of the CLIPs core can be seen in the intermediate stages of the process. One can also observe gradual growth of the twisted spikes.

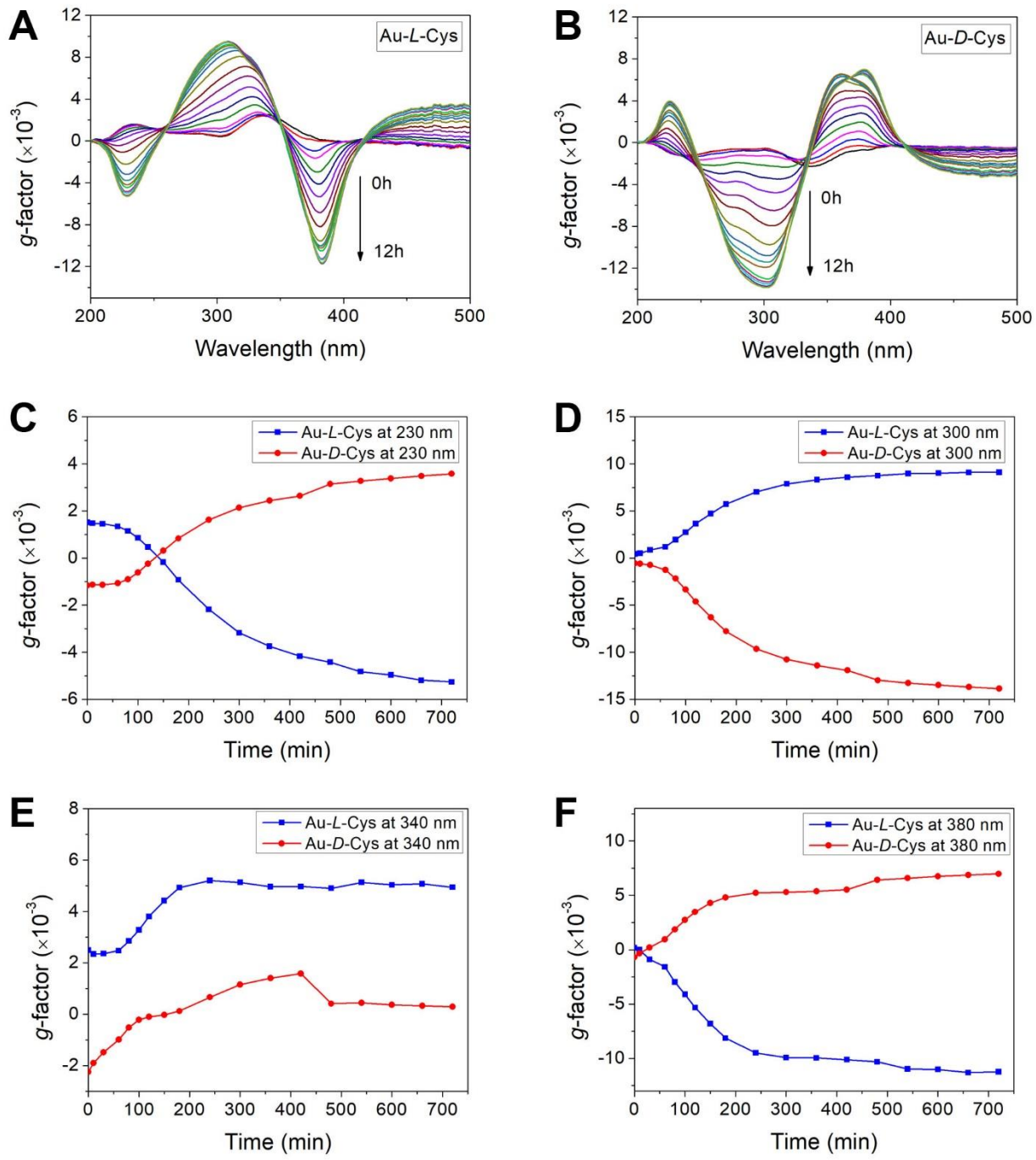

Figure S12. Time series of CD spectra of gold-cysteinate nanoplatelets as they assemble into CLIPs. A,B, CD spectra evolution of Au-*L*-Cys (A) and Au-*D*-Cys (B) solution from initially mixing reagents together (time: 0 h) to reaction for 12 h. (**C** to **F**) Asymmetry factor of absorbance (*g*-factor) dependence on time at wavelength of 230 nm (C), 300 nm (D), 340 nm (E) and 380 nm (F).

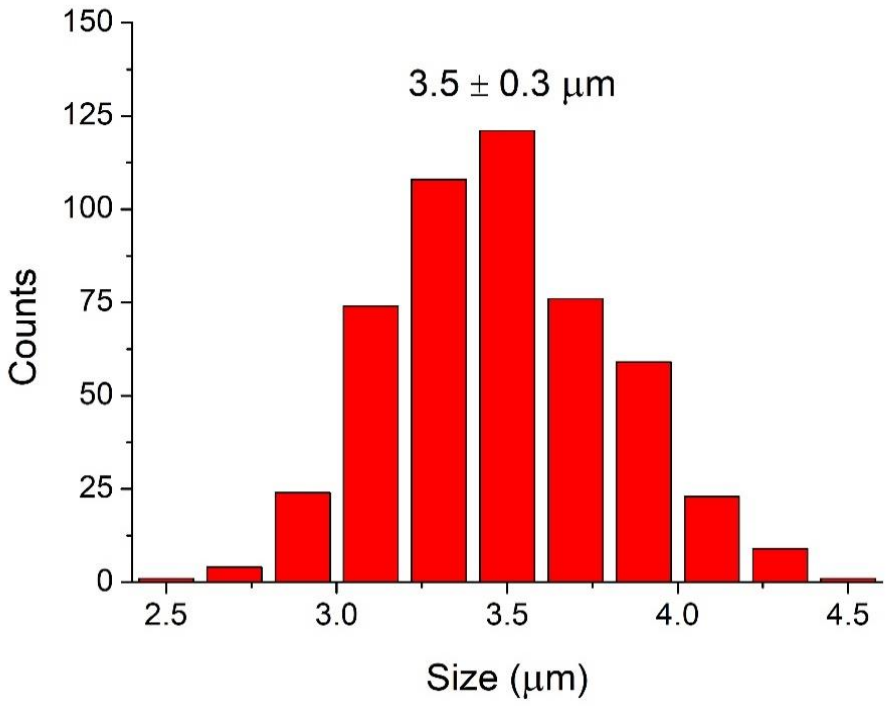

Figure S13. Size distribution of 500 Au-*L*-Cys CLIPs.

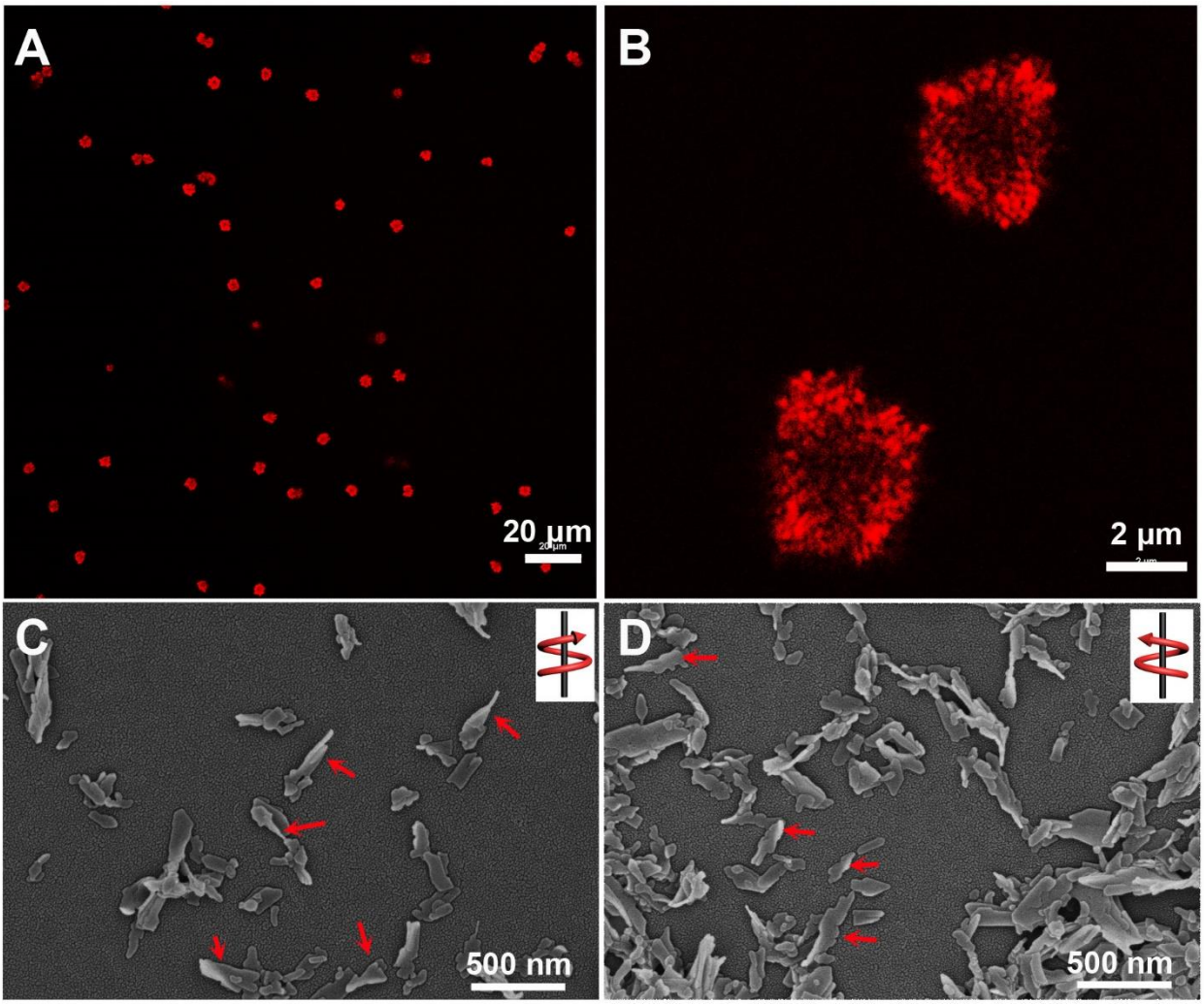

Figure S14. Microscopy data for CLIPs. A,B, Confocal microscopy of Au-*D*-Cys CLIPs registering intrinsic red light emission of the CLIPs. **C,D,** SEM images of Au-*L*-Cys CLIPs (C) and Au-*D*-Cys CLIPs (D) after 15 min of sonication. Assemblies are broken down into separated or small bundles of twisted ribbons. Red arrows in (C) and (D) show individual twisted ribbons.

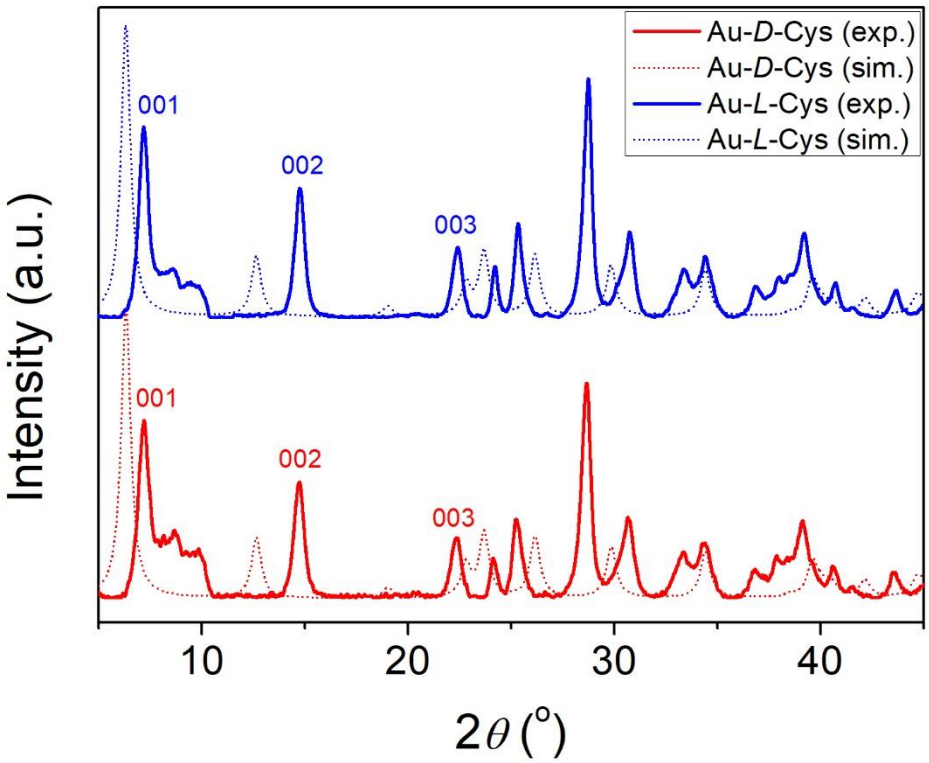

Figure S15. XRD spectra of Au-Cys CLIPs. Acquired XRD data from Au-Cys CLIPs (*L*- and *D*- form) is compared with the proposed atomic lattice model in Figure S2A. The layered structure of the assemblies is interpreted by the [001], [002] and [003] peaks corresponding to *d*-spacings of 12.3 Å, 6.1 Å and 3.0 Å, respectively. Simulated XRD peaks calculated using the model obtained in MD calculations similar to **Figure 1N, O, P** match with the characteristic peaks in the experimental data. Experimental data shows peaks with smaller inter-planar *d*-spacings as compared to simulated data, which is attributed to the freeze-drying method for preparation of XRD sample.

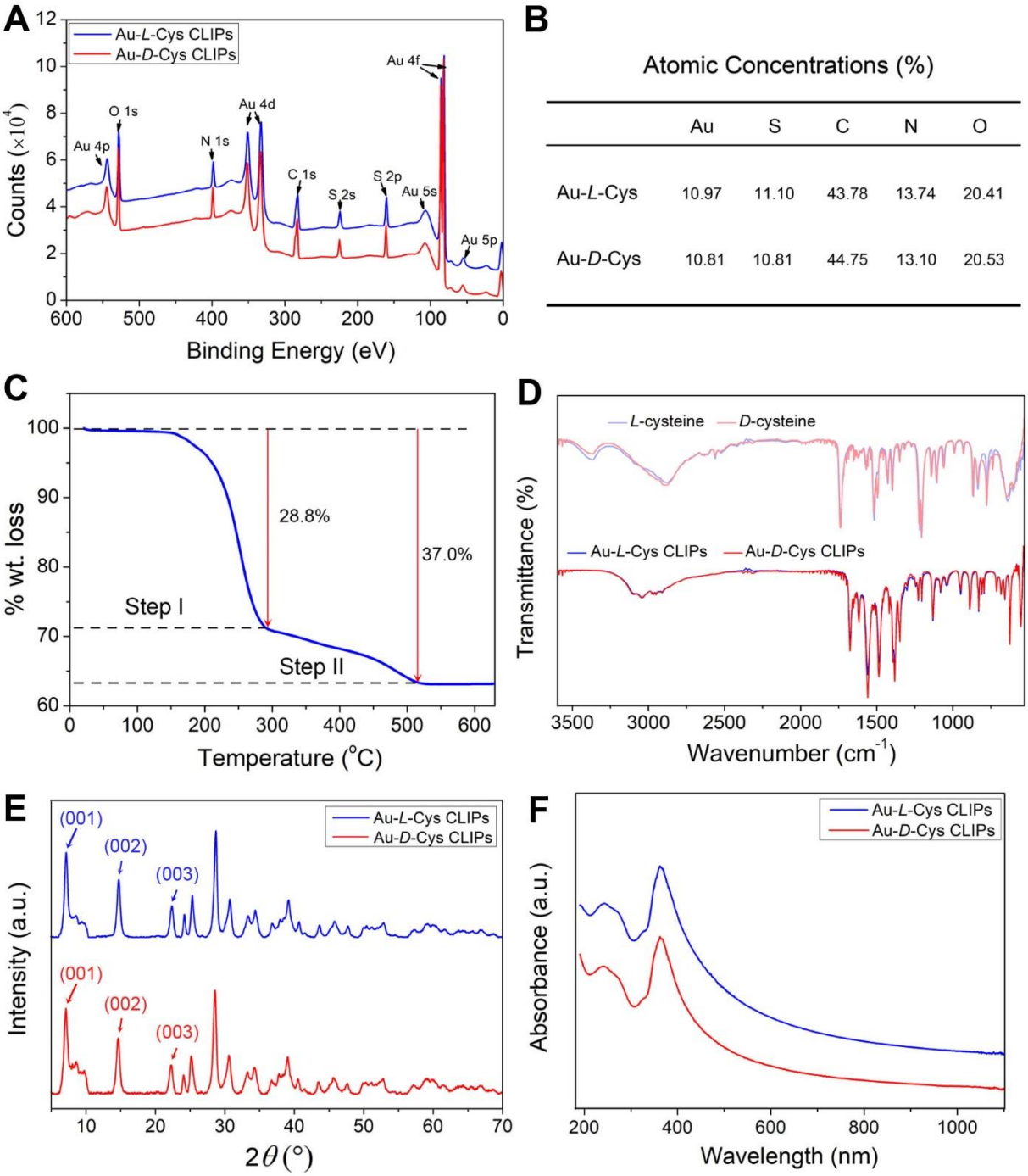

Figure S16. Chemical characterizations of Au-*L*-Cys (blue) and Au-*D*-Cys (red) HOPs. A, XPS wide-range spectra of Au-*L*-Cys (blue) and Au-*D*-Cys (red). **B,** Atomic concentrations of Au, S, C, N, O in Au-Cys obtained from XPS spectra. Au-*L*-Cys and Au-*D*-Cys contain gold, sulfur, nitrogen, carbon and oxygen corresponding to equal amount of Au atoms and Cys residues and is consistent with lamellar gold thiolates (fig. S2A). Each data point was averaged over four measurements. **C,** Thermogravimetric analysis (TGA) of CLIPs. The mass decrease for Step I and Step II of decomposition corresponds to the cysteine content of the Au-Cys nanosheets. The weight percentage of Au atoms of ~63% observed by TGA matches the Au content of ~62% calculated for gold cysteinate sheets (fig. S2A). **D,** Fourier-transform infrared

spectroscopy (FTIR) spectra of CLIPs. The absence of a peak at 2562 cm^{-1} in CLIPs, corresponding to the S-H vibrations, indicates the formation of S-Au bonds. **E,** X-ray diffraction (XRD) of CLIPs. [001] reflection at 7.2° indicated that the product has a lamellar structure with a layer thickness of 1.23 nm. **F,** UV-vis spectra of CLIPs (curves are vertically shifted to improve clarity). Monocrystallinity of twisted ribbons forming CLIPs engenders a sharp absorption peak at 362 nm and strong red fluorescence associated with the ligand-to-metal charge transfer (LMCT, S→Au) transition. The luminescence originates from the singlet states of the two-dimensional gold-sulfur networks.

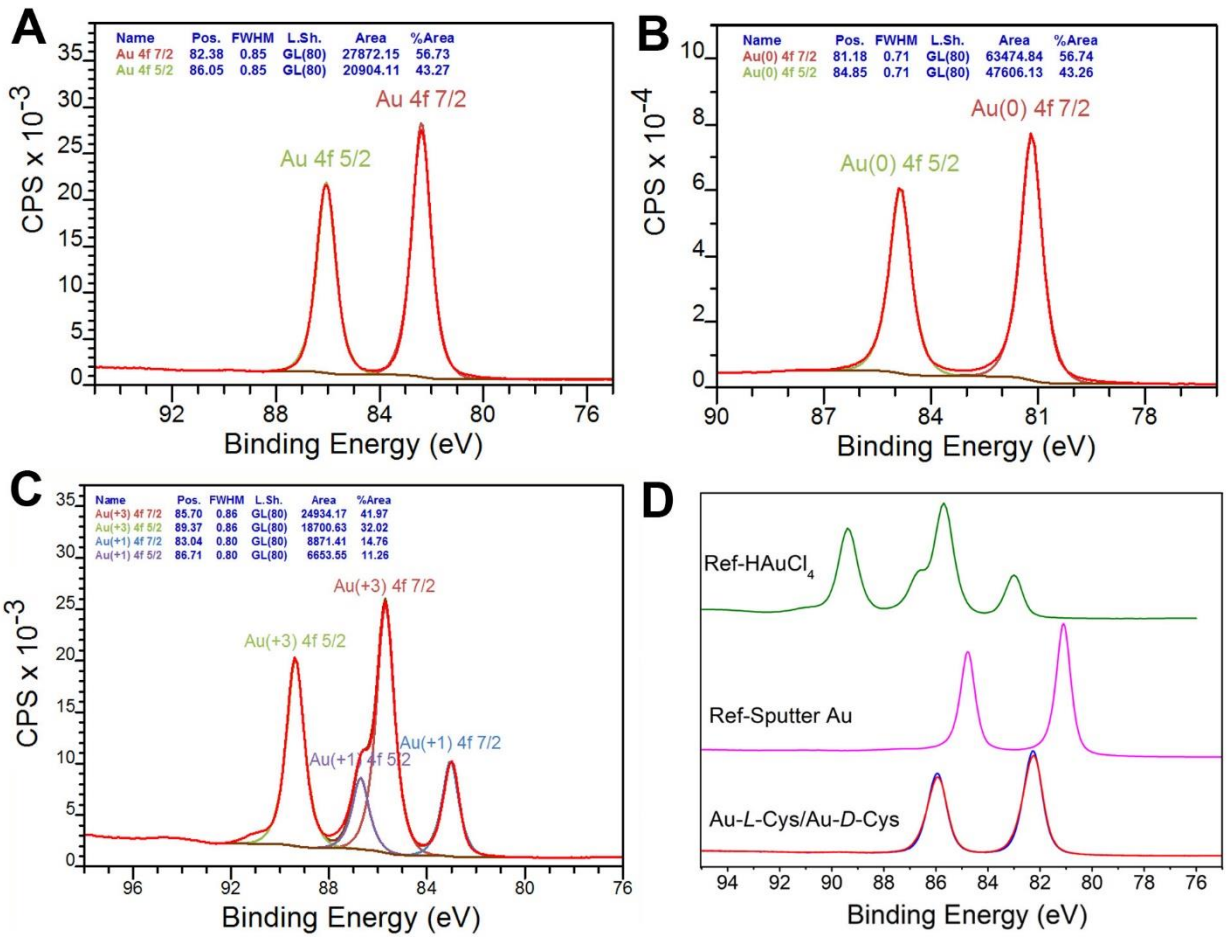

Figure S17. X-ray photoelectron spectroscopy (XPS) spectra of Au-Cys CLIPs and related Au compounds in Au 4f region. A, Au-*L*-Cys CLIPs indicates that the oxidation state of gold in the CLIPs is between 0 and +1 (*19*), which is fully consistent with the structure of gold cysteinate in Figure S2A. **B,** Freshly sputtered gold film. **C,** $HAuCl_4 \cdot 3H_2O$. The Au 4f 7/2 peak at 85.7 eV is assigned to Au(III), while the other pair with the Au 4f 7/2 peak at 83.04 eV is assigned to Au(I). The difference of 2.66 eV is a characteristic energy difference between Au(III) and Au(I). **D,** The comparison between Au 4f peaks of Au-Cys with reference data for Au(0), Au(I) and Au(III).

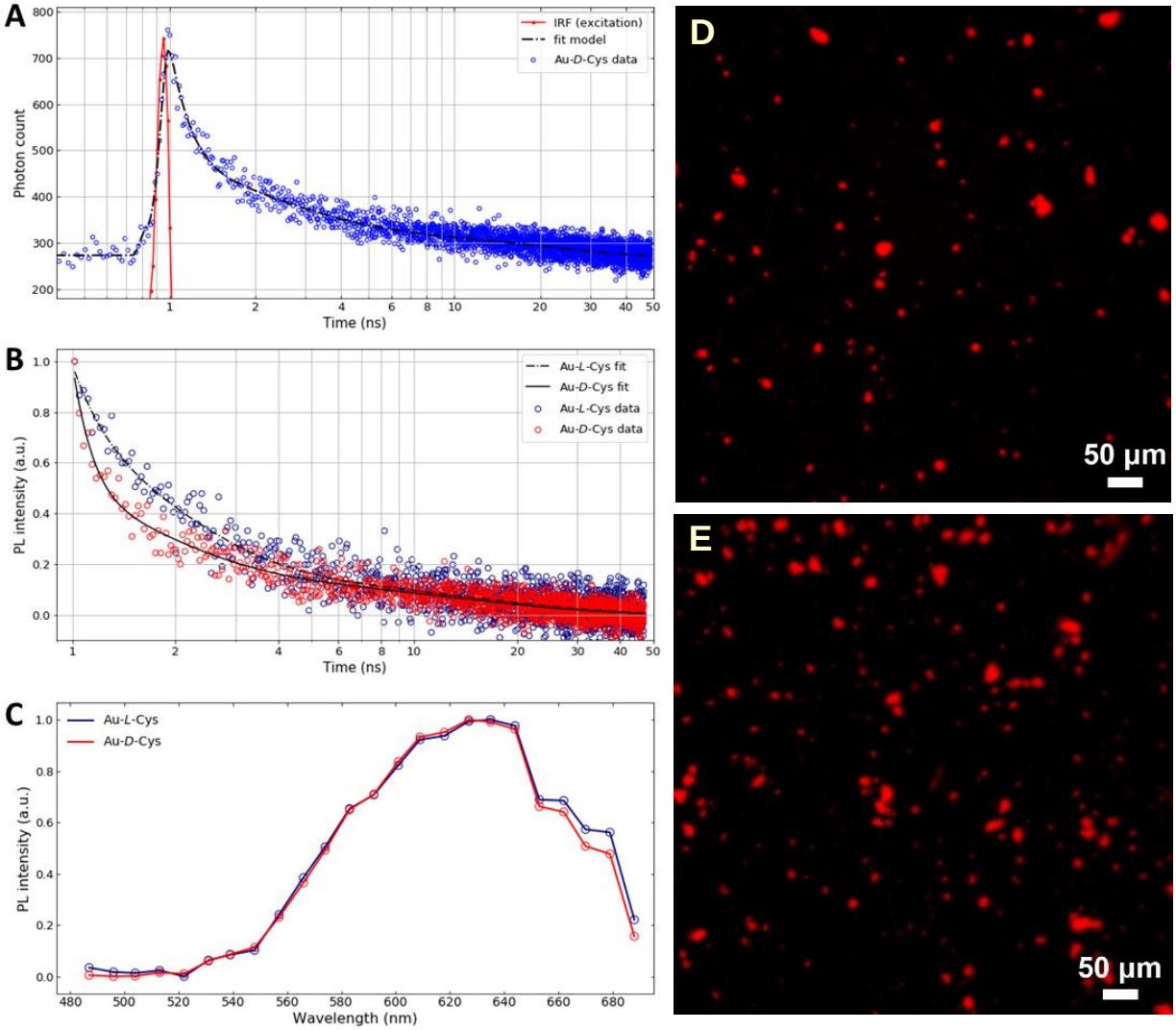

Figure S18. Fluorescence time-resolved microscopy (FLIM) and spectroscopy of CLIPs. A, Time-resolved photon counts for Au-*D*-Cys CLIPs excited by a 405 nm laser pulses. Blue circles correspond to single-photon counts after the emitted fluorescence passes through a 650 nm optical band-pass filter (FWHM is 40 nm). The instrument resolution function (IRF, *i.e.* excitation laser pulse profile) is shown by red trace. **B,** Comparison of the fluorescence decay curves for Au-*L*-Cys and Au-*D*-Cys CLIPs with the double exponential fit of the fluorescence dynamics $\boldsymbol{f(t) = A_1 \cdot \exp(-t/\tau_1) + A_2 \cdot \exp(-t/\tau_2)}$. The fitting parameters [A_1, τ_1 (ns), A_2, τ_2 (ns)] for Au-*L*-Cys CLIPs and Au-*D*-Cys CLIPs are [1.83, 1.01 ns, 0.21, 13.2 ns] and [4.14, 0.52 ns, 0.22, 11.4 ns], respectively. **C,** Emission spectra of Au-*L*-Cys CLIPs (blue) and Au-*D*-Cys CLIPs (red) measured by fluorescence confocal microscopy with laser excitation at 405 nm. **D,E,** Confocal microscopy images of Au-*L*-Cys (D) and Au-*D*-Cys (E) CLIPs.

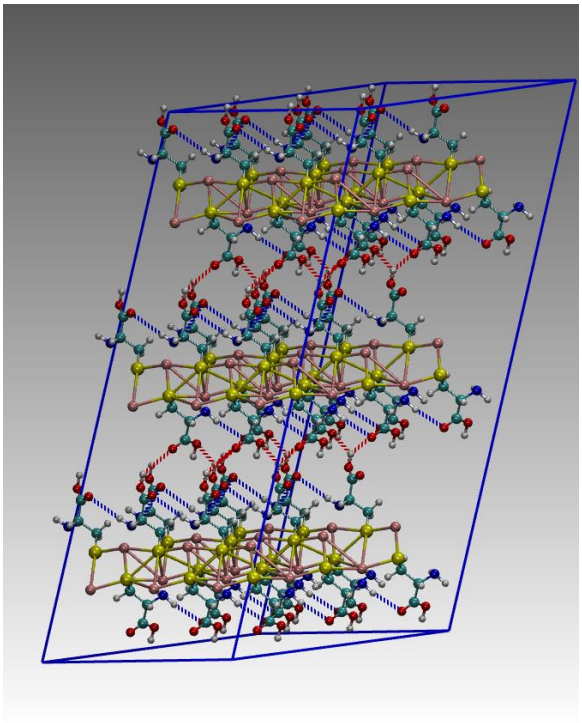

Figure S19. MD-DFT models of stacked Au-*L*-Cys nanosheets. The calculations were performed for a unit cell comprising two units of Au-*L*-Cys, but a supercell with dimensions 3x3x3 is shown here to improve clarity regarding the packing patterns within and between layers (dashed lines depict the hydrogen bonds formed between different cysteine ligands). The calculations were performed using CP2K software (version 5.1) with the MOLOPT basis set and the GTH pseudopotential. A full geometry optimization was performed, followed by 3.5 ps of molecular dynamics simulation in the NPT ensemble (T=300 K; P = 1 bar).

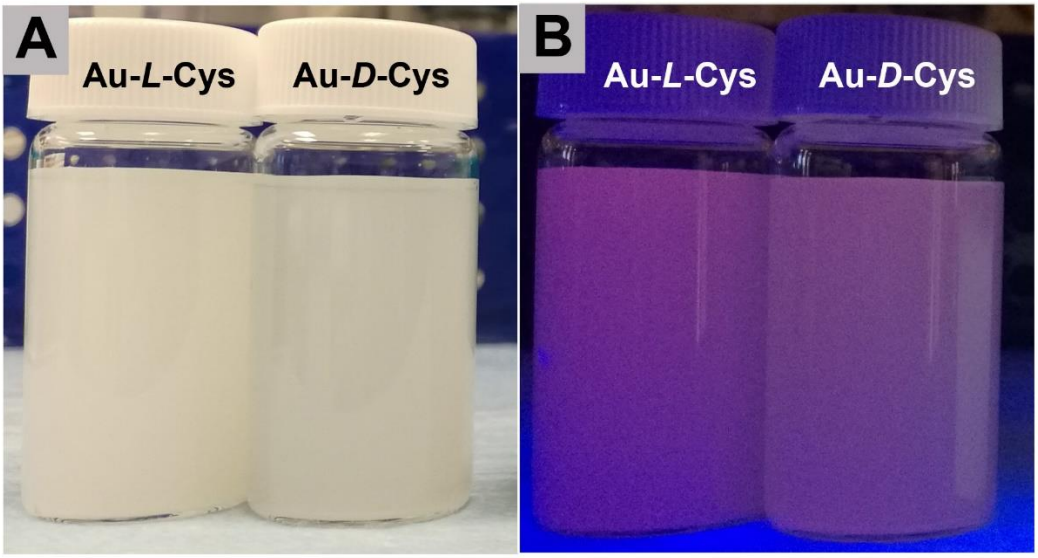

Figure S20. Colloidal stability of Au-Cys CLIPs aqueous dispersions. Photographs of Au-Cys CLIPs dispersions under daylight (**A**) and UV light (**B**) after standing for 1 h.

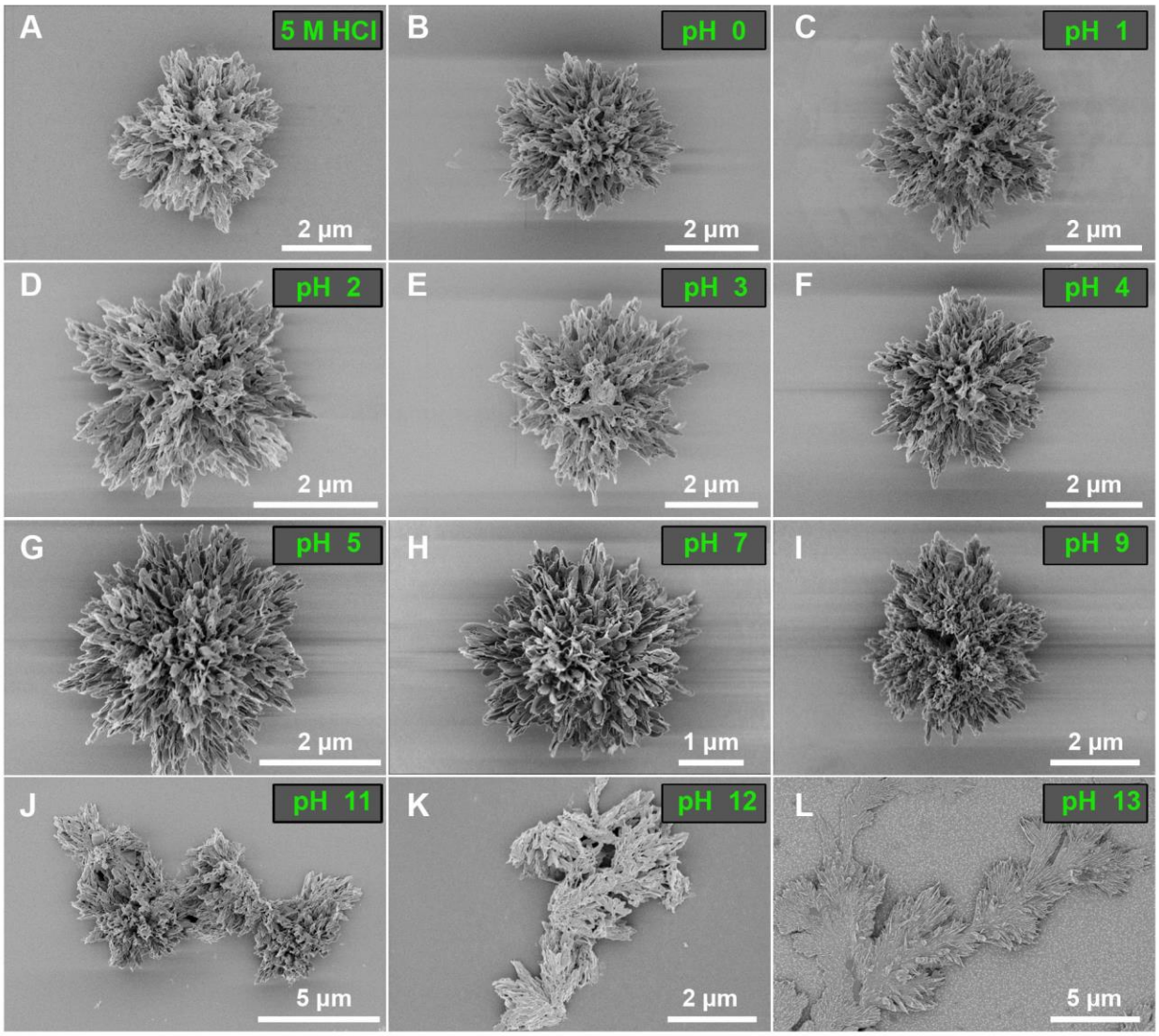

Figure S21. Scanning electron microscopy images of Au-*L*-Cys CLIPs in different pH after 12 h. The values of pH in micrographs **A** to **L** are given in the green font. Au-Cys CLIPs retained their spiky morphology from extreme acidic (5M HCl) to highly basic conditions (~ pH 11). At pH over 11 (including 2M and 5M NaOH), CLIPs gradually disassemble into simpler HOPs, other fragments or they even decompose. The SEM background in (L) represents NaOH residue on the substrate.

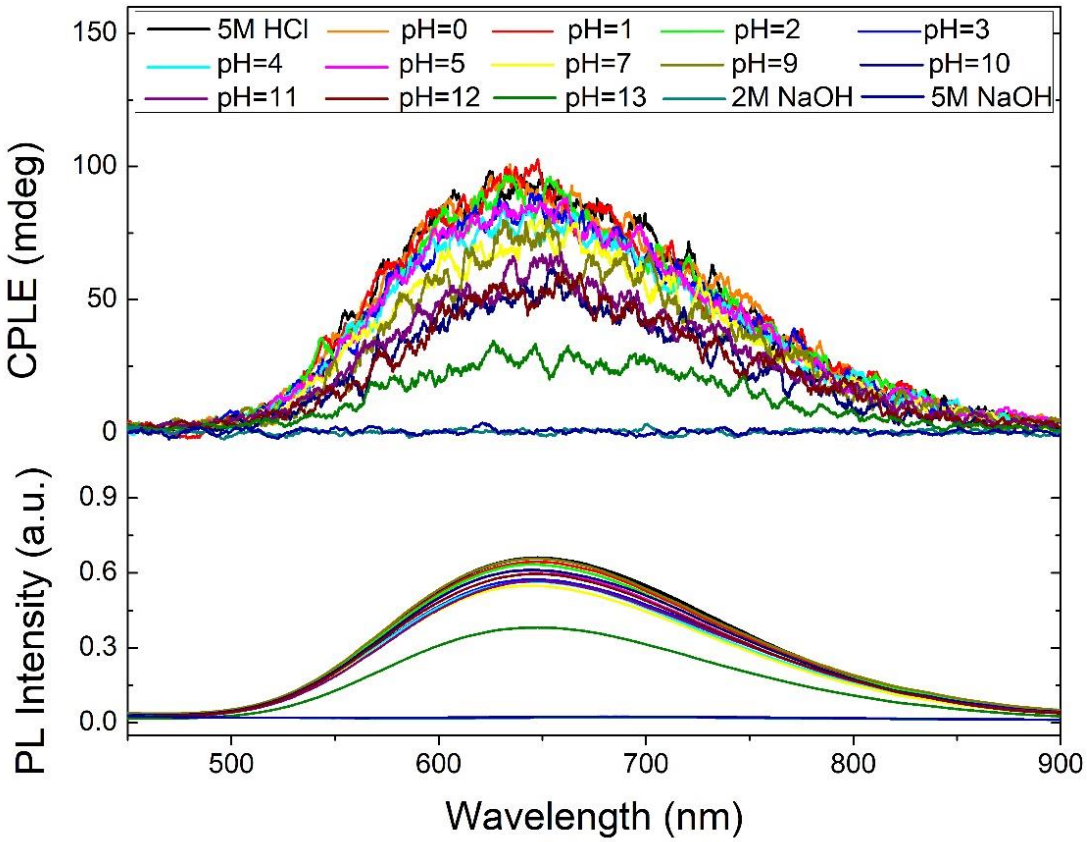

Figure S22. CPLE spectra of Au-*L*-Cys CLIPs exposed to different pH for 12 h. From extreme acidic conditions corresponding to 5M HCl to strongly basic conditions corresponding to pH 11, Au-*L*-Cys CLIPs dispersions retained a positive CPLE indicating the coccolith-like spiky geometry (Fig. S21). At extreme basic conditions corresponding to 2 M and 5M NaOH, the red emission and CPLE disappears. The sign of CPLE is defined by the micron and submicron scale chirality of the assembled structure and not by the emitted state as in the traditional circularly-polarized luminescence.

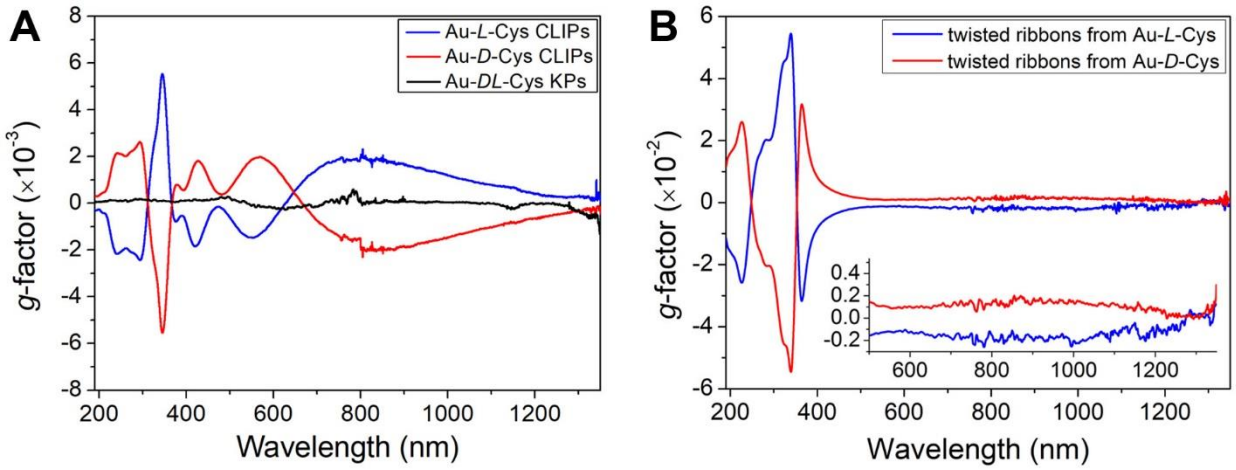

Figure S23. Circular polarization anisotropy g-factor of Au-Cys CLIPs and individual twisted ribbons. A, *g*-factor of Au-*L*-Cys (blue), Au-*D*-Cys (red) CLIPs and Au-*DL*-Cys (black) kayak particles. **B,** *g*-factor of Au-*L*-Cys (blue), Au-*D*-Cys (red) after sonication.

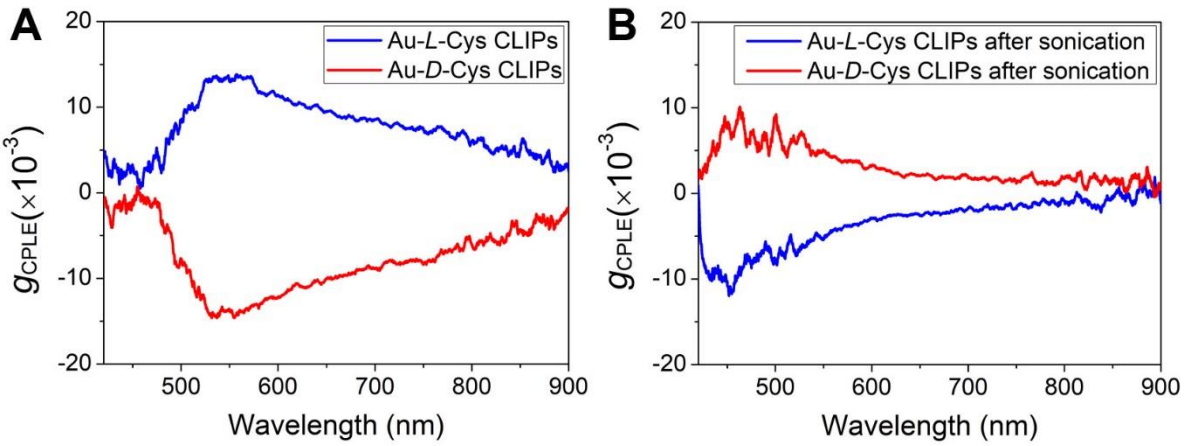

Figure S24. CPLE optical anisotropy factor, g_{CPLE} for Au-Cys CLIPs and constituent nanoribbons. g_{CPLE} (**A**) before and **(B)** after sonication resulting in the disassembly of CLIPs into nanoribbons. The maximum g_{CPLE} of the CLIPs is ~0.015, which is larger than typical values observed for molecules and NPs. The maximum g_{CPLE} of the individual ribbons is smaller, ~ 0.01, which is consistent with the decrease of scattering. The opposite sign of CPLE of nanoribbons corresponds to their opposite handedness compared to the stack of nanoribbons forming spikes in CLIPs.

The photon of 620 nm light emitted from Au-S-Cys sheets are circularly polarized because they are emitted by chiral electronic states. This conclusion is supported by the fact that even disassembled ribbons from CLIPs are CPL-active (fig. S24B). This mechanism is associated with the angstrom-scale chirality of the excited states in the Au-S-Cys nanosheets.

The second mechanism is differential scattering of emitted photons on chiral particles after the emissive event. The strong evidence for the contribution of this mechanism is found in the fact that the polarization direction of photons emitted from the sample is reversed in CLIPs (fig. S24A) compared with the disassembled ribbons (fig. S24B). This mechanism is associated the submicron scale chirality of the assembled particles.

After the emission of photons, their polarization can be changed to opposite one due to scattering of these photons off the dispersed particles. Depending on the size of the particles and their shape the extent of this secondary polarization rotation changes. Therefore, the sign of the circularly polarized light can be the same as the original one or change to the opposite one. For hedgehog particles that rotate the polarization strongly, it become opposite. For nearly straight nanoribbons, that do not have strong helicity, it remains the same as the original ones.

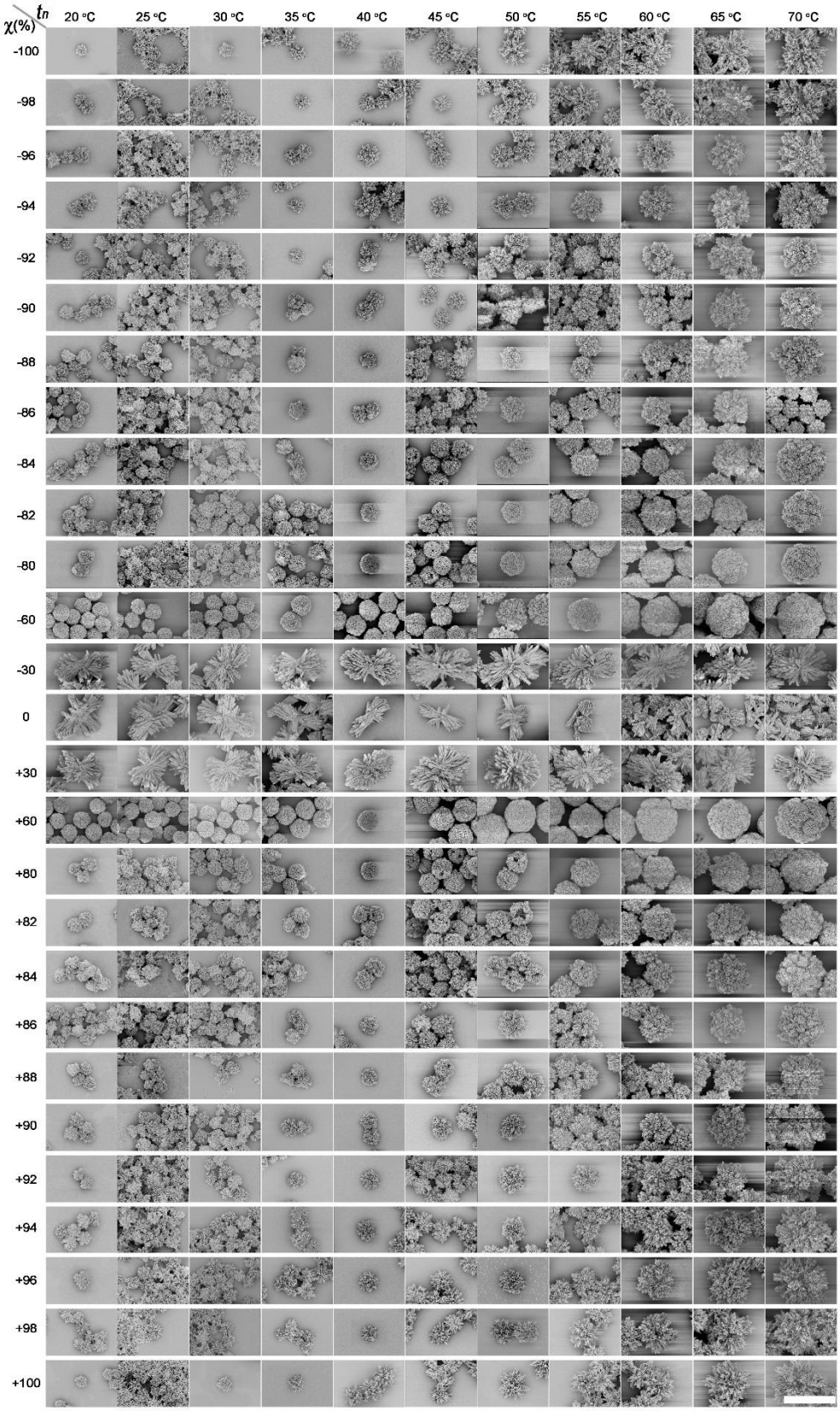

Figure S25. Full set of SEM images of Au-Cys particles assembled for different building block nucleation temperatures, t_n and χ. Scale bar: 6 μm.

Table S3. GT representations and *CI* values for different complex particles

Particle Image	Particle Designation	GT-model	*CI* value	*CI* Formula	Model Comments; URL
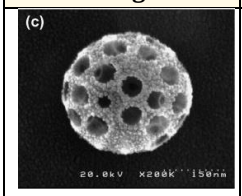	Porous spherical supraparticle from NPs	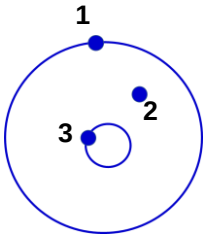	**4**	**N1** = 2 **N2** = 0 **N3** = 2 **CI** = 2+0+2 = 4	The central loop depicts the randomly distributed pores. The node in the loop denotes the self-assembly of NPs forming a supraparticle. (https://doi.org/10.1016/j.apt.2013.11.004). (*41*)
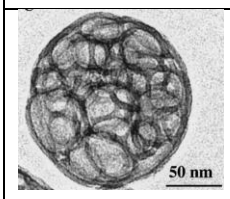	Prorous particle from nanosheets	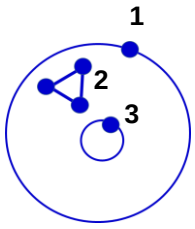	**8**	**N1** = 2 **N2** = 2+(2*2)/2 = 4 **N3** = 2 **CI** = 2+4+2 = 8	The central loop depicts the randomly distributed pores. They are multiple and disordered similarly to porous spherical supraparticles. The constituent units of these particles, are however, thin nanosheets of silica denoted by the K_3 model between the loops. They do not have any specific order and thus, are not connected to loops. (https://doi.org/10.1016/S0022-3093(01)00434-3). (*42*)
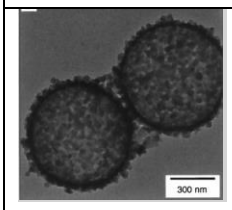	Templated nanoshells from NPs	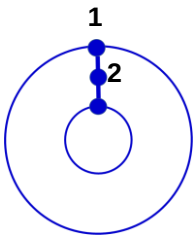	**9.75**	**N1** = 3 + (2/2) + (3/4) = 4.75 **N2** = 2 + (2*3)/2 = 5 **CI** = 4.75 + 5 = 9.75	The nanoshell morphology denoted as two loops connected by a node to designate that there is only single open space in the particle, not randomly distributed pores as in porous spherical supraparticles. The shell is made from a layer of individual NPs designated as K_1 module, *i.e.* a node. (https://doi.org/10.1126/science.282.5391.1111). (*43*)
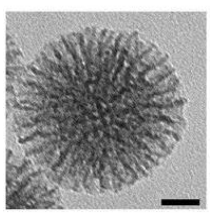	Supraparticle with radial pores	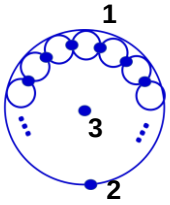	**14**	**N1** = 4 + $\sum_{n=1}^{\infty}\frac{2*4}{2^n}$ = 12 **N2** = 2 **N3** = 0 **CI** = 12 + 2 + 0 = 14	Pores are partially organized but particles are not. The pore is denoted by the loop with the empty internal space. Each pore shares some particles with adjacent pore. (https://doi.org/10.3390/molecules24020332). (*44*)
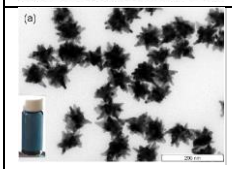	Irregular nanostars with metakic spikes	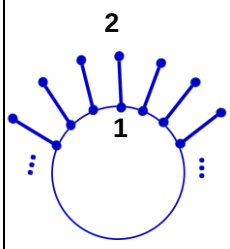	**16.5**	**N1** = 3 + (2*3+1)/2 + $\sum_{n=2}^{\infty}\frac{2*3+2*1}{2^n}$ = 10.5 **N2** = 1 + 3/2 + (2*3)/4 + $\sum_{n=3}^{\infty}\frac{2*3+2*1}{2^n}$ = 6 **CI** = 10.5 + 6 = 16.5	The particle has a continuous gold core and spikes. The core is described by a single loop without any nanoscale constituent in it. The spikes are made of continuous gold phase, and have approximately linear shape. Thus, they are represented by multiple K_2 graphs. (https://www.mdpi.com/2073-4344/3/1/288). (*45*)

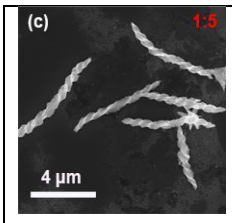	Helices from NP braided chains	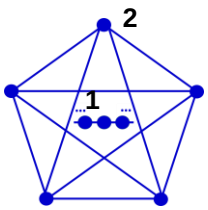	**18**	**N1** = 2 + $\sum_{n=1}^{\infty} \frac{2*2}{2^n}$ = 6 **N2** = 4 + (4*4)/2 = 12 **CI** = 6 + 12 = 18	The shape of the particles here is helical, and thus it is represented by the K_5 graph replacing the previous loops. The NP inside the helices are organized in chains containing multiple NPs, which is represented by the graph used in Figure S26 g and h to denote NP chains. (https://doi.org/10.1021/acs.chemmater.9b04143). (*46*)
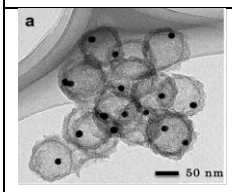	Yolk-shell particle with single NP in the central pore	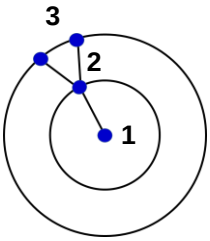	**20.75**	**N1** = 1 + 5/2 + (2*3)/4 = 5 **N2** = 5 + (1+2*3)/2 = 8.5 **N3** = 3 + (3+5)/2 + 1/4 = 7.25 **CI** = 5 + 8.5 + 7.25 = 20.75	The high *CI* in this case corresponds to high degree of control over the structure of these particles. There is always a single NP core denoted by the connected node inside the central loop. Furthermore, there is always a single nanosheet forming the shell represented by the connected K_3 module between two loops. (https://doi.org/10.1063/1.4902435). (*47*)
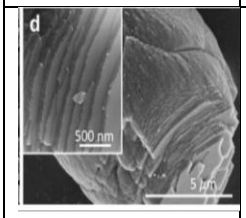	Layered supraparticle from nanosheets	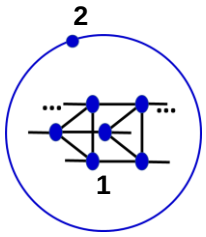	**26**	**N1** = 4 + (4*4)/2 $\sum_{n=2}^{\infty} \frac{6*4}{2^n}$ = 24 **N2** = 2 **CI** = 24 + 2 = 26	The constitutive units of this particles are nanosheets. They are organized in a layered structure, hence the K_3 units are connected. The large number of stacked nanosheets give progression of gradually decreasing components of the sum. (https://doi.org/10.3390/nano9050798). (*48*)
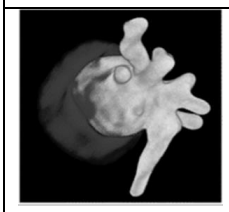	Janus nanostars	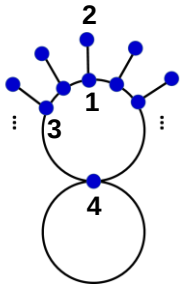	**38.25**	**N1** = 3 + (2*3+1)/2 + $\sum_{n=2}^{\infty} \frac{2*3+2*1}{2^n}$ = 10.5 **N2** = 1 + 3/2 + (2*3)/4 + $\sum_{n=3}^{\infty} \frac{2*3+2*1}{2^n}$ = 6 **N3** = 3 + (4+3+1)/2 + (2*3+1)/4 + $\sum_{n=3}^{\infty} \frac{2*3+2*1}{2^n}$ = 10.75 **N4** = 4 + (2*3)/2 + $\sum_{n=2}^{\infty} \frac{2*3+2*1}{2^n}$ = 11 **CI** = 10.5 + 6 + 10.75 + 11 = 38.25	The core particle is a solid silica particle that is described as a single loop. There are no nodes or constituent modules inside the loop because it is a continuous inorganic phase. The gold spikes are localized on one side designated by the second loop. The spikes are approximately linear continuous gold nanostructures. Thus, they are represented by a multiple K_2 unit. (https://doi.org/10.1039/C3CC47531J). (*49*)

Table S4. Various GT indices for complex particles listed in Table S3

Table S4. Various GT indexes for complex particles listed in Table S3							
Particle Description	***CI***	**Avg. degree**	**Graph density**	**Modularity**	**Avg. Clustering Coeff.**	**Avg. Betweeness Centrality**	**Avg. Closeness Centrality**
Porous spherical supraparticle from NPs	4.00	1.33	0.67	N/A	N/A	N/A	N/A
Porous particle from nanosheets	8.00	2.00	0.50	0.00	1.00	0.00	0.60
Templated nanoshells from NPs	9.75	2.67	1.33	0.00	0.33	0.33	0.78
Mesoporous Silica	14.00	3.82	0.38	0.36	0.00	7.27	0.33
Irregular star	16.50	2.00	0.11	0.55	0.00	25.00	0.37
Helices from NP chains	18.00	2.53	0.18	0.55	0.39	8.00	0.52
Yolk-shell	20.75	3.00	1.00	0.08	0.72	0.50	0.78
Layered Supraparticles	26.00	3.74	0.13	0.58	0.20	43.55	0.24
Janus star	38.25	2.00	0.20	0.39	0.00	7.73	0.40

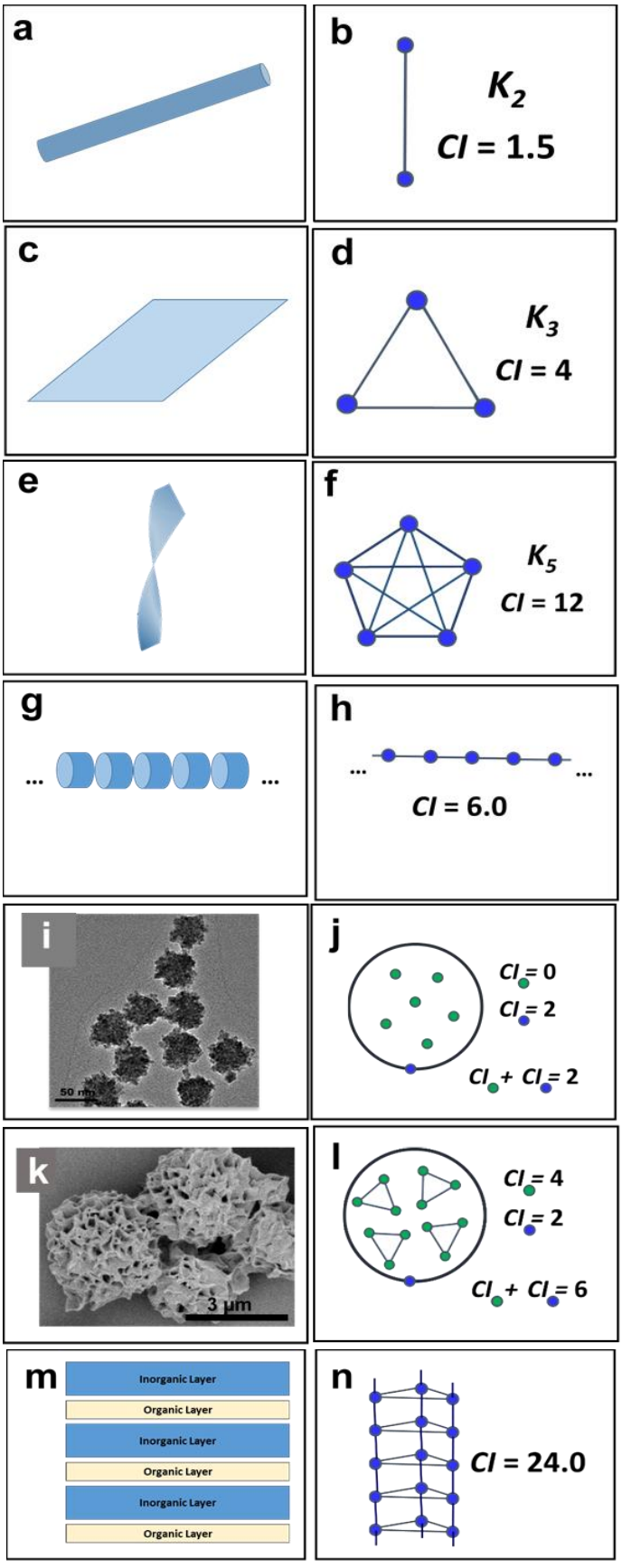
a
b
K_2
CI = 1.5
c
d
K_3
CI = 4
e
f
K_5
CI = 12
g
...
...
h
...
...
CI = 6.0
i
50 nm
j
CI_i = 0
CI_i = 2
CI_i + CI_i = 2
k
3 µm
l
CI_i = 4
CI_i = 2
CI_i + CI_i = 6
m
Inorganic Layer
Organic Layer
Inorganic Layer
Organic Layer
Inorganic Layer
Organic Layer
n
CI = 24.0

Figure S26. Graph theory models (GT-models) of basic self-assembled structures. a,b, Pictorial representation of self-assembled nanowire and (**b**) its GT-model; **c,d,** Pictorial representation of self-assembled nanosheet and (**d**) its GT-model; **e,f,** Pictorial representation of self-assembled twisted ribbon and (**f**) its GT-model; **g,h,** Pictorial representation of self-assembled chain of individual nanoparticles and (**h**) its GT-model. **i,j,** SEM image of supraparticle from CdSe nanoparticles (from Ref. (*23*)) and (**j**) its GT-model. **k,l,** SEM image of supraparticle from Au-TGA/*L*-Cys (9:1) nanosheets and (**l**) its GT-model; **m,n,** Pictorial representation of nacre-like nanocomposites and (**n**) their GT-model.

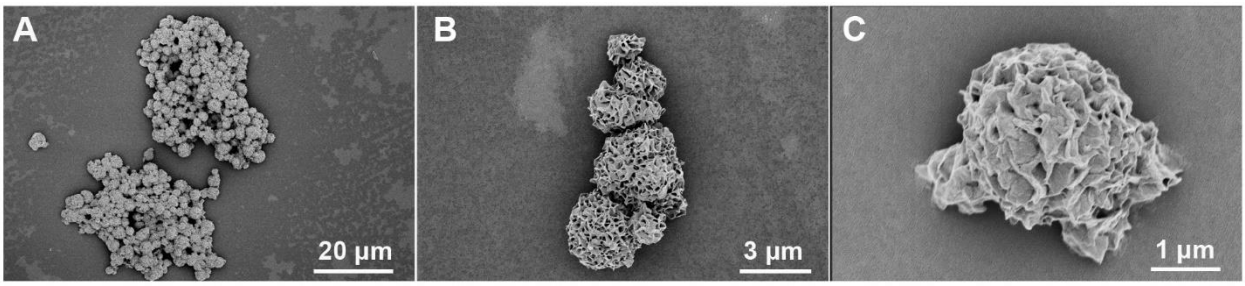

Figure S27. SEM images at different magnifications of assemblies from nanoparticles with thioglycolic acid (TGA) as surface ligands. Gold thioglycolate (Au-TGA) assemblies at low (**A** and **B**) and (**C**) high magnifications.

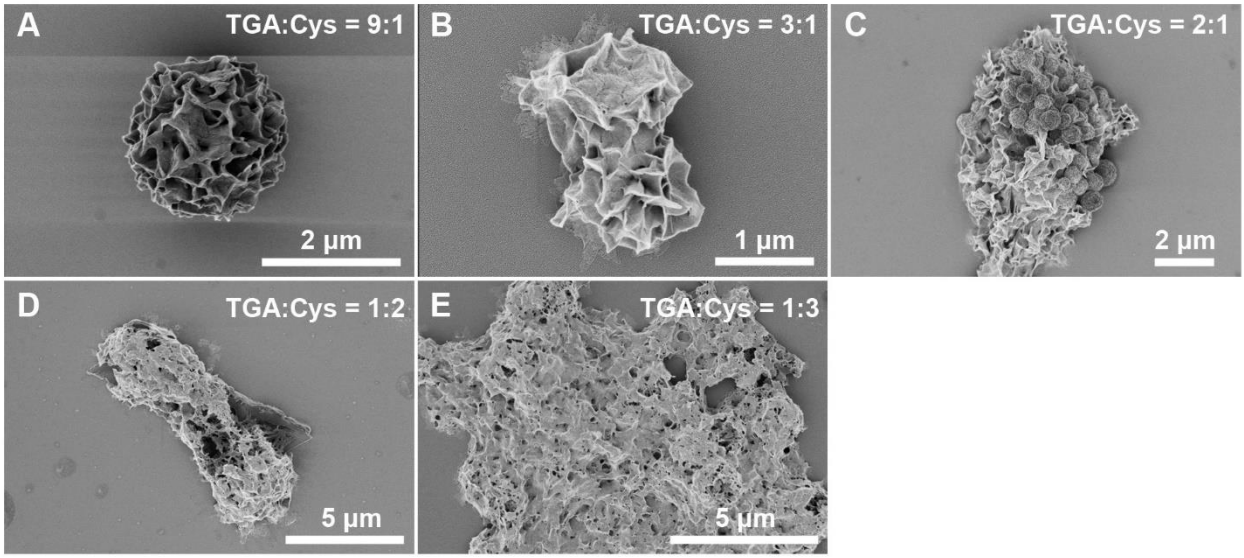

Figure S28. SEM images of structures prepared with different TGA and *L*-Cys ratios. All these particles represent low-χ phases. The change from CLIPs (**Figure 1,** main text) to high-mass disordered states (fig. S1) when TGA:Cys = 1:3 depicts the transition from order to disorder particularly well. For high TGA content, such as TGA:Cys = 9:1, the self-limitation of the particle growth due to electrostatic repulsion is stronger than for other ratios of surface ligands. *CI* of the supraparticle in (A) is 6.0 (see **Figure 4, A** and **B**, GT Methods). The post-assembly recrystallization, which may be associated with additional porosity and complexity, does not change the overall shape of the assembled structures and the symmetry elements characteristic of initial particles.

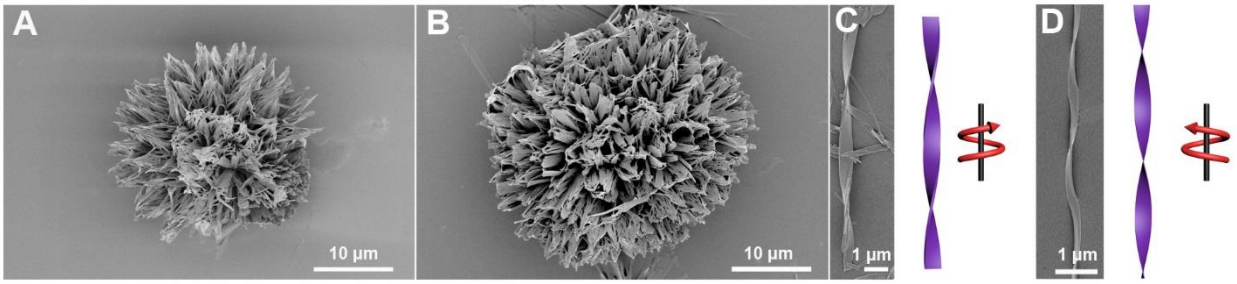

Figure S29. Au-Pen CLIPs prepared with penicillamine as ligand under conditions identical to those in Figure 1. A,B, SEM images of Au-*L*-Pen (A, prepared with *L*-enantiomer) and Au-*D*-Pen (B, prepared with *D*-enantiomer) CLIPs. **C,D,** individual twisted ribbons of Au-*L*-Pen (C) and Au-*D*-Pen (D) obtained after sonication. The twisted ribbons forming in case of *L*- and *D*-Pen display the same handedness as those formed for *L*- and *D*-Cys. The synthesis of Au-Pen CLIPs was conducted under the same conditions as those of Au-Cys CLIPs.

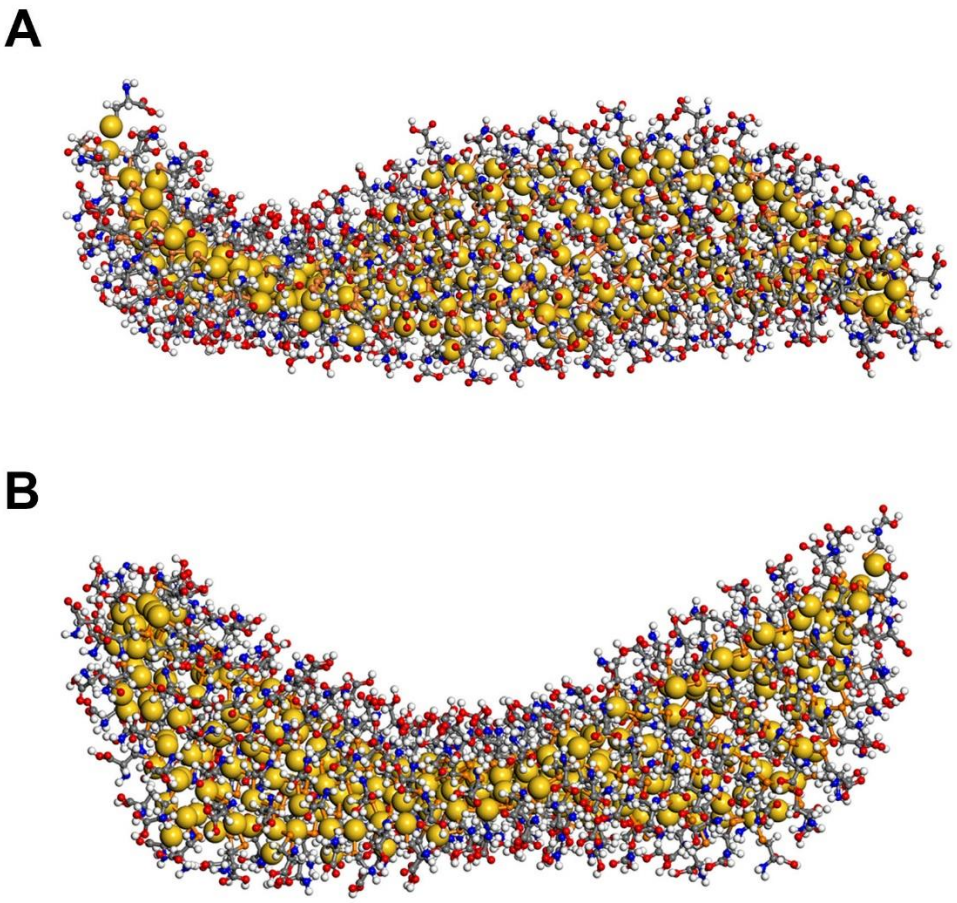

Figure S30. Shapes of the short ribbons for (A) Au-*L*-Cys and (B) Au-*D*-Cys serving as building blocks for CLIPs and other HOPs.

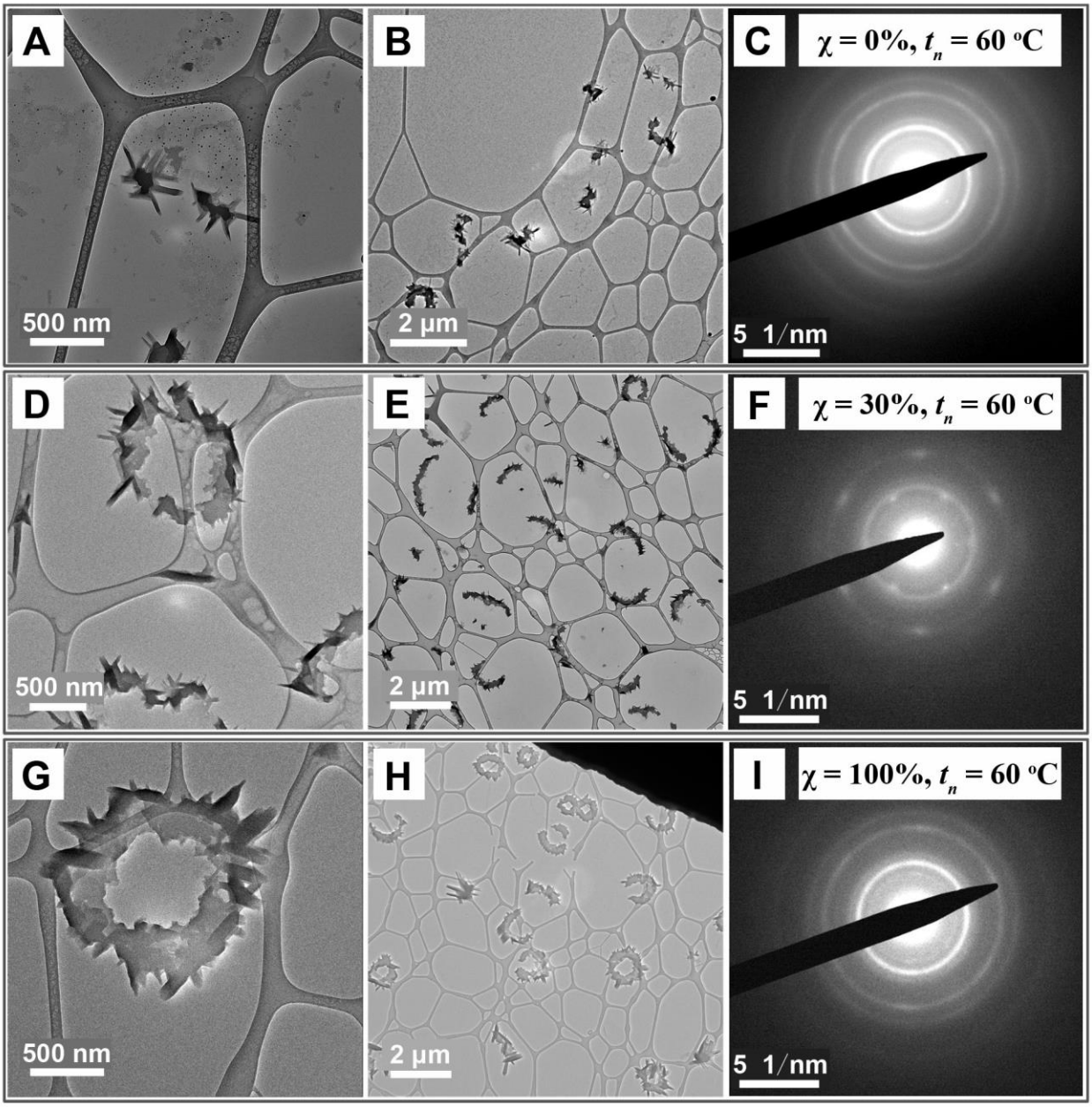

Figure S31. **Early HOPs forming for differ**ent χ obtained after 1 min after initiation of the self-assembly: (**A** to **C**) kayak particles; (**D** to **F**) BB2; and (**G** to **I**) CLIPs.

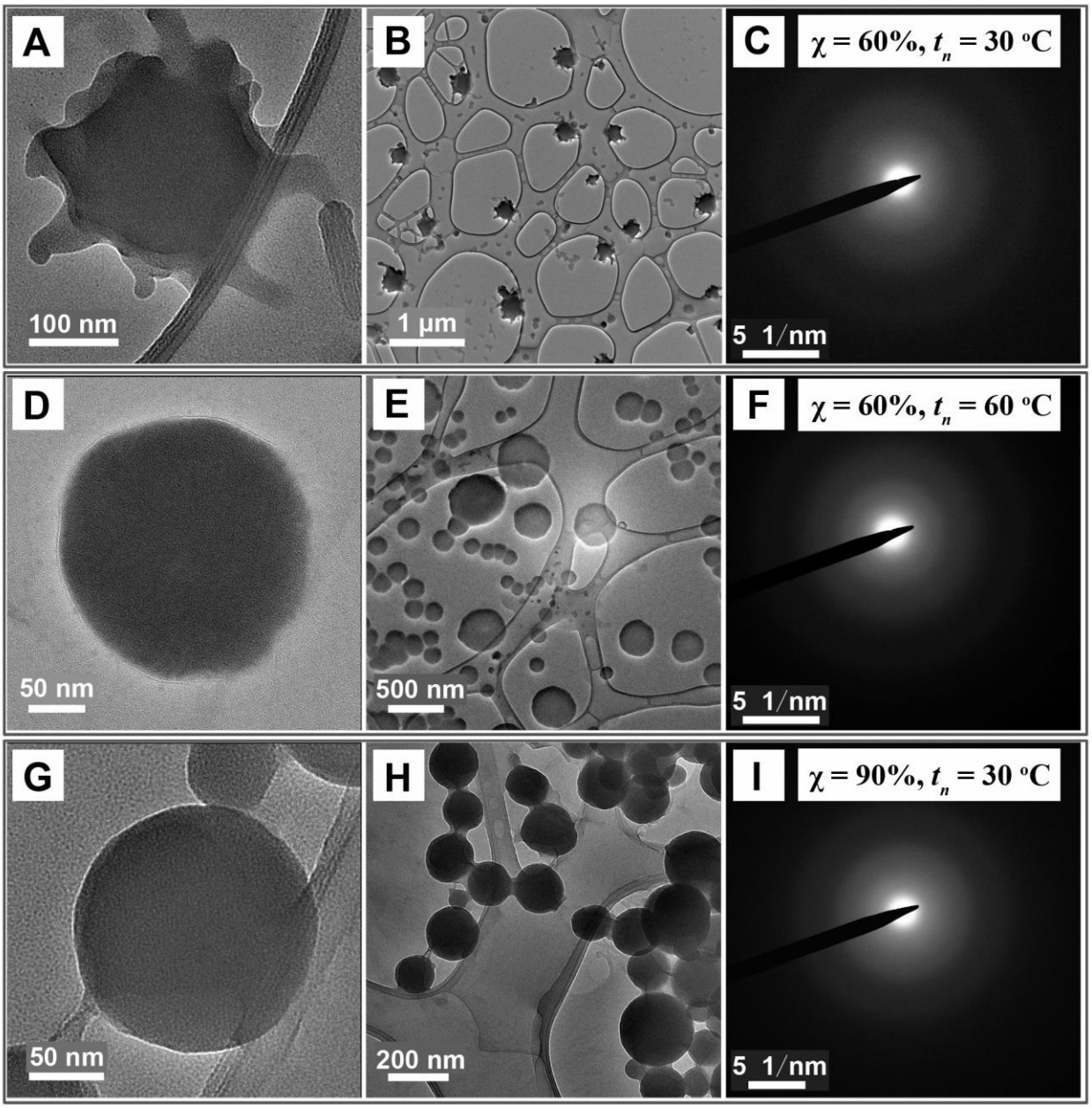

Figure S32. **Early building blocks and assemblies for SPP1, SPP2, and DSP phases** in fig. S25 at different magnifications obtained after 1 min after initiation by mixing of corresponding ***Solutions A*** and ***D***: (**A** to **C**) SPP1; (**D** to **F**) SPP2; and (**G** to **I**) DSP.

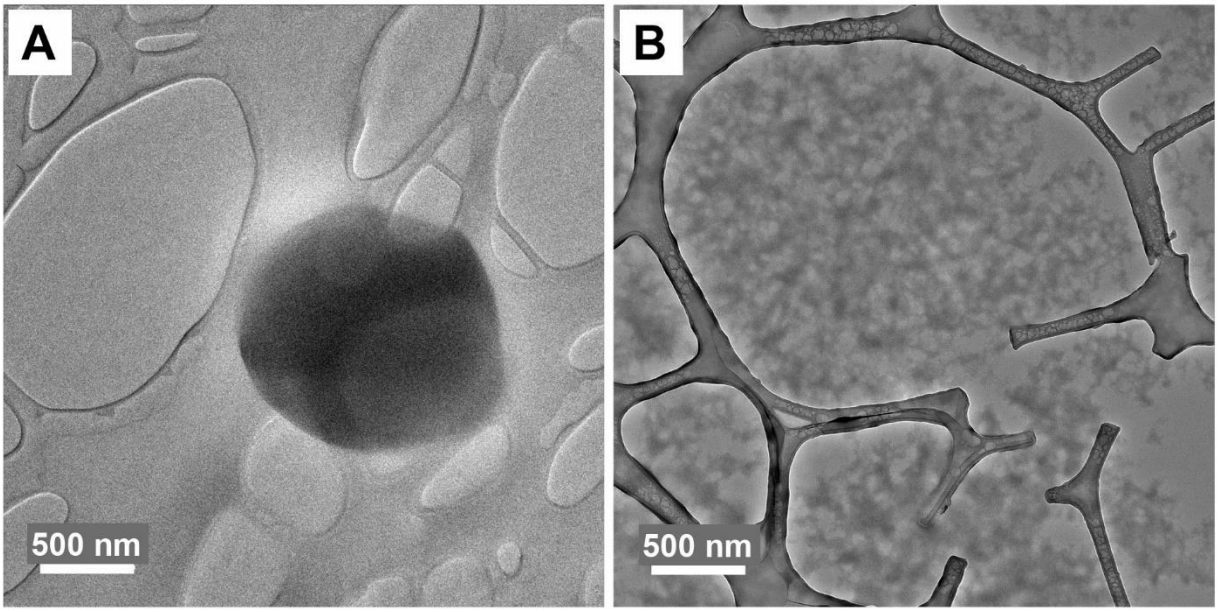

Figure S33. **Building blocks of nanoassemblies with TGA/*L*-Cys 9:1 forming the spheroidal supraparticles shown in fig. S28.**

Figures S31-S33 indicate that there is conservation of the elements of symmetry between the building blocks and the resulting assemblies. The same effect can also be traced in other assemblies of nanoparticles, such as chiral CdTe tetrahedrons and planar graphene quantum dots (*40, 46*).

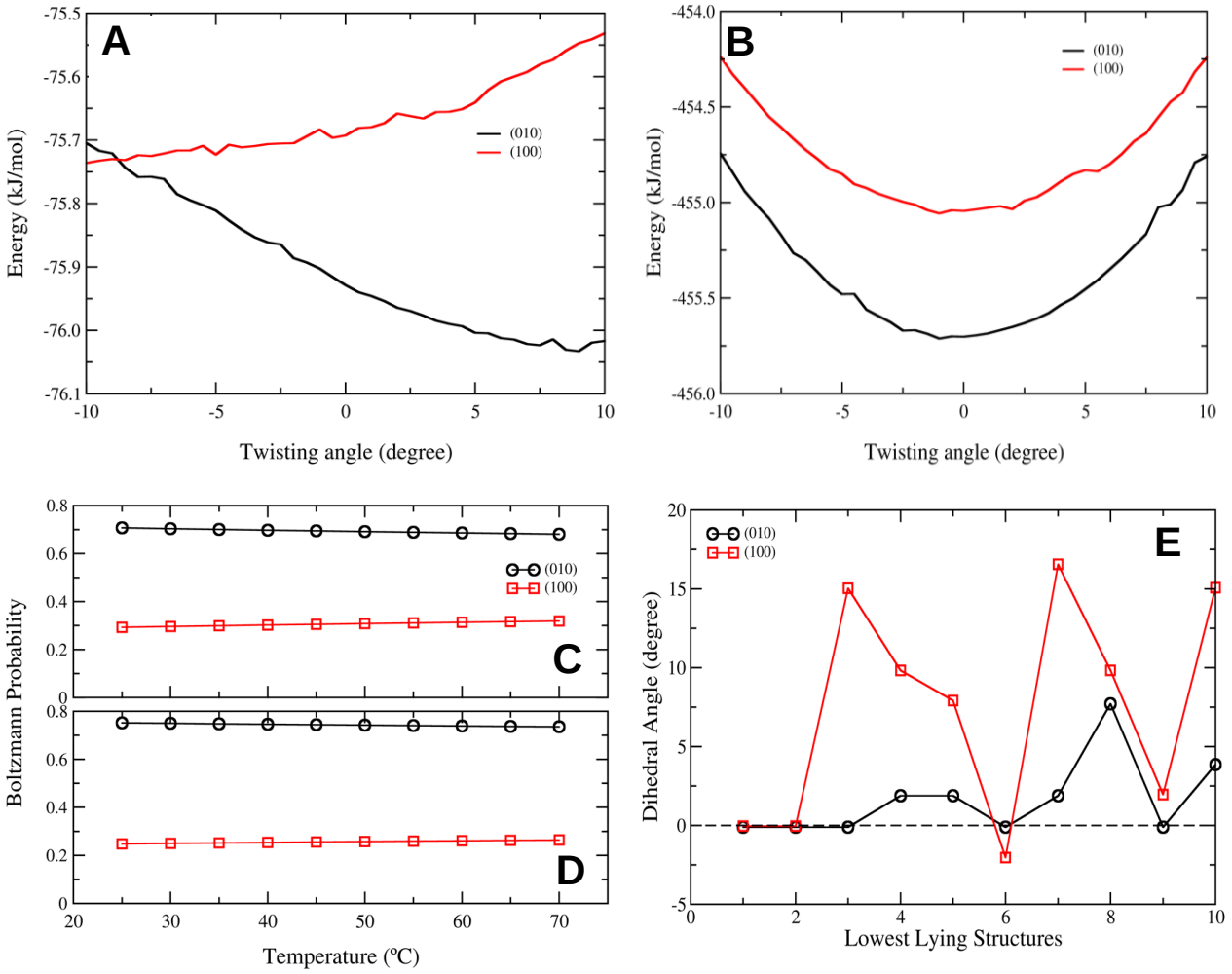

Figure S34. Thermodynamic characteristics of nanoplatelets dependent on crystal structure and temperature obtained by coarse-grained molecular mechanics calculations. (A) Electrostatic and **(B)** elastic (Lennard-Jones) energy components *per* $(Au\text{-}S)_2$ unit for the torsion of the Au-Cys nanoplatelets around their longer axis. The energetic asymmetry of the torsion arises from the long-ranged electrostatic interactions between the charged groups rather than by short-ranged dispersion interactions, although the latter determine the greater stability of the sheet growing in the [010] direction as compared to those growing in [100] direction. The dispersion interactions behave as an elastic restoring force, while the electrostatic interactions behave as chiral forces favoring one sense of rotation. **C,D,** Relative thermodynamic stability for the ten lowest-lying dimers of Au-*L*-Cys sheets with crystallographic orientations [010] and [100]: **(**C**)** stacking of sheets in the [001]; **(**D**)** oriented attachment of sheets along their preferential growth direction. The largest thermodynamic stability for both the face-to-face and the edge-to-edge growth is again found for [010] platelets. **E,** Dependence of the relative orientation between the two Au-*L*-Cys sheets defined by the dihedral angle between the nanoplatelets for the ten lowest-energy structures (see Methods). Face-to-face assembly of the nanoplatelets has a large probability of forming twisted stacks. However, addition of CTAB (see Methods) makes the system favor the edge-to-edge assembly.

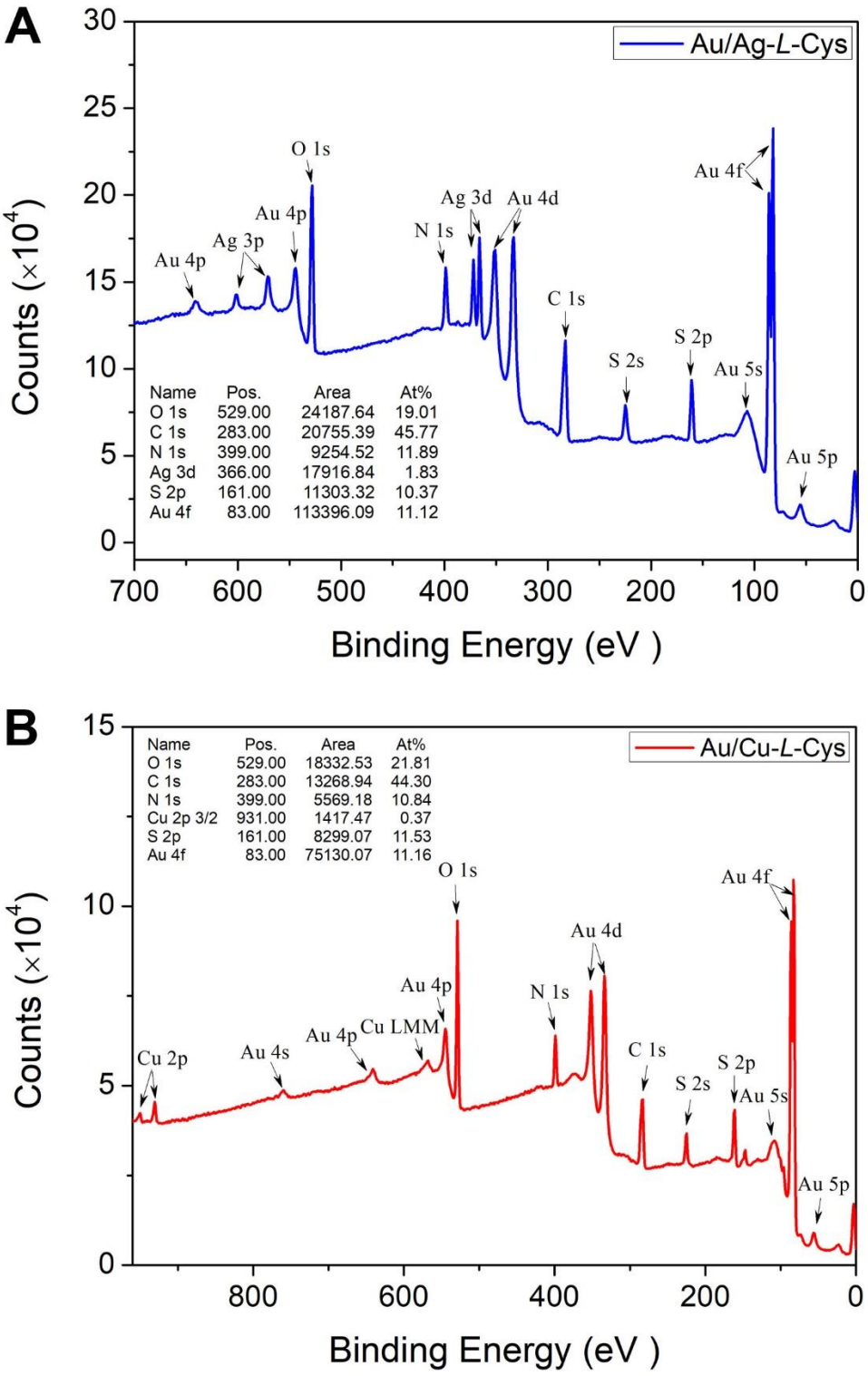

Figure S35. XPS spectra of (A) Au/Ag-Cys and (B) Au/Cu-Cys HOPs. The molar ratio between Ag or Cu to Au is 16.5% and 3.3%, respectively, calculated from XPS results. It is notable that the ratio of Ag or Cu to Au was 17.4% and 17.3%, respectively, when the self-assembly was carried out.

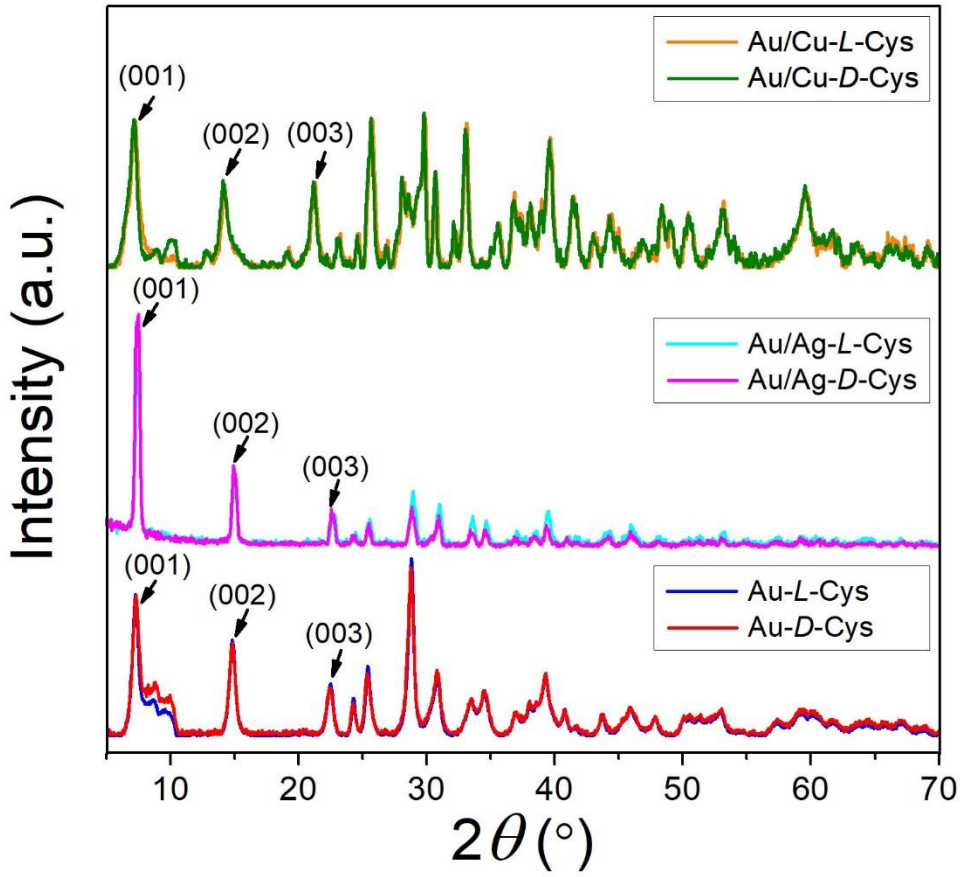

Figure S36. XRD spectra of Au/Cu-Cys, Au/Ag-Cys and Au-Cys. All NP assemblies show periodic peaks (00w, *w* = 1,2,3) indicating the lamellar structure corresponding to formation of assembled nanosheets.

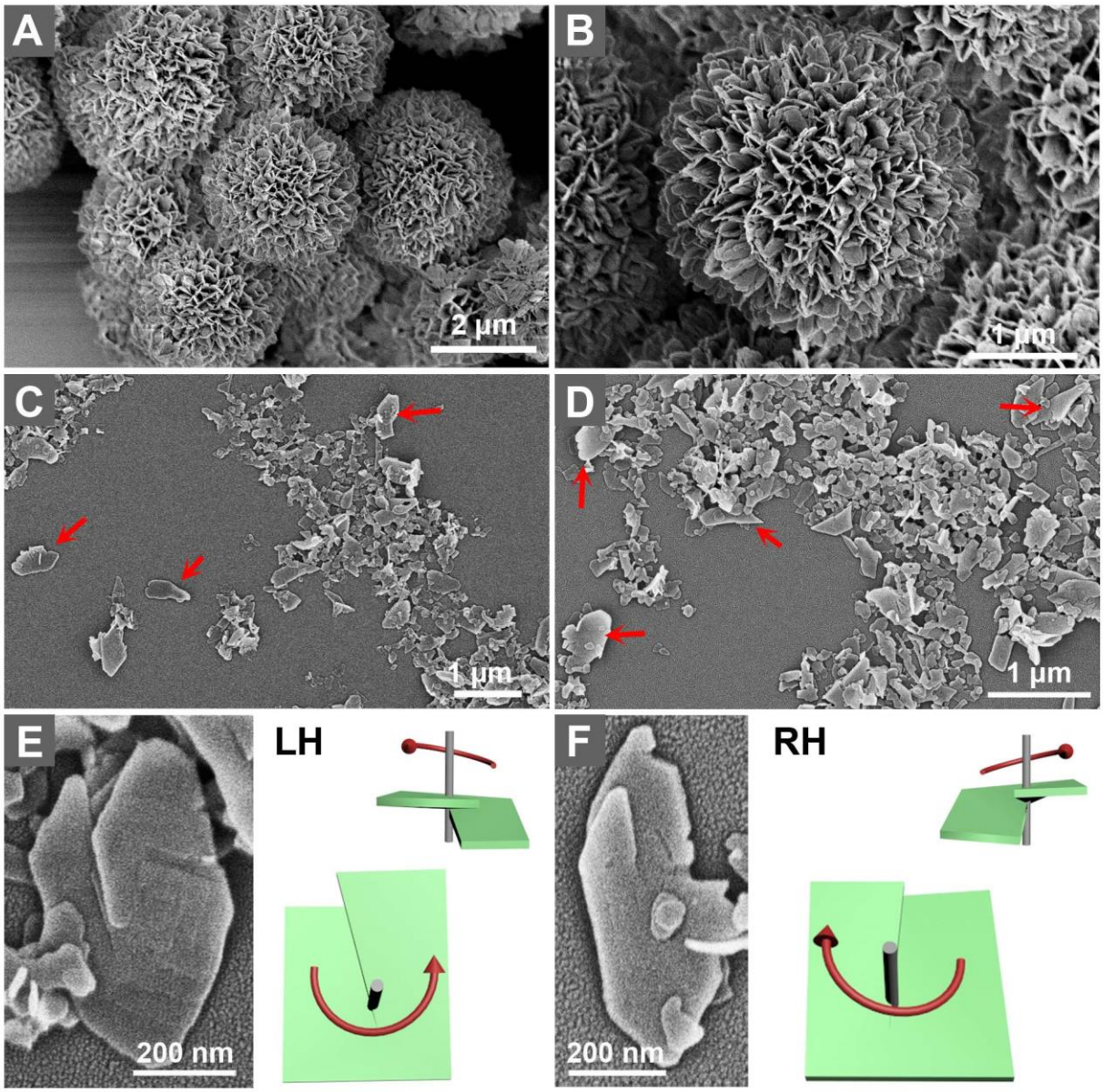

Figure S37. SEM images of Au/Cu-Cys assemblies. A,B, Au/Cu-*L*-Cys HOPs before sonication. **C,** Au/Cu-*L*-Cys and **D,** Au/Cu-*D*-Cys fragments after sonication. **E,F,** Helical stacks of nanoribbons of Au/Cu-*L*-Cys (E) and Au/Cu-*D*-Cys (F). Red arrows in (C) and (D): Nanosheets of a characteristic size greater than 500 nm display chiral geometries with geometries consistent with screw dislocations in different directions (E and F). The change in geometry is related to the increase of nanosheet stiffness and corresponding drastic increase of twisting energy. The characteristic energy associated with dislocations of individual nanoplatelets with respect to each other is much smaller and can be estimated to be 40-140 kJ/mol.

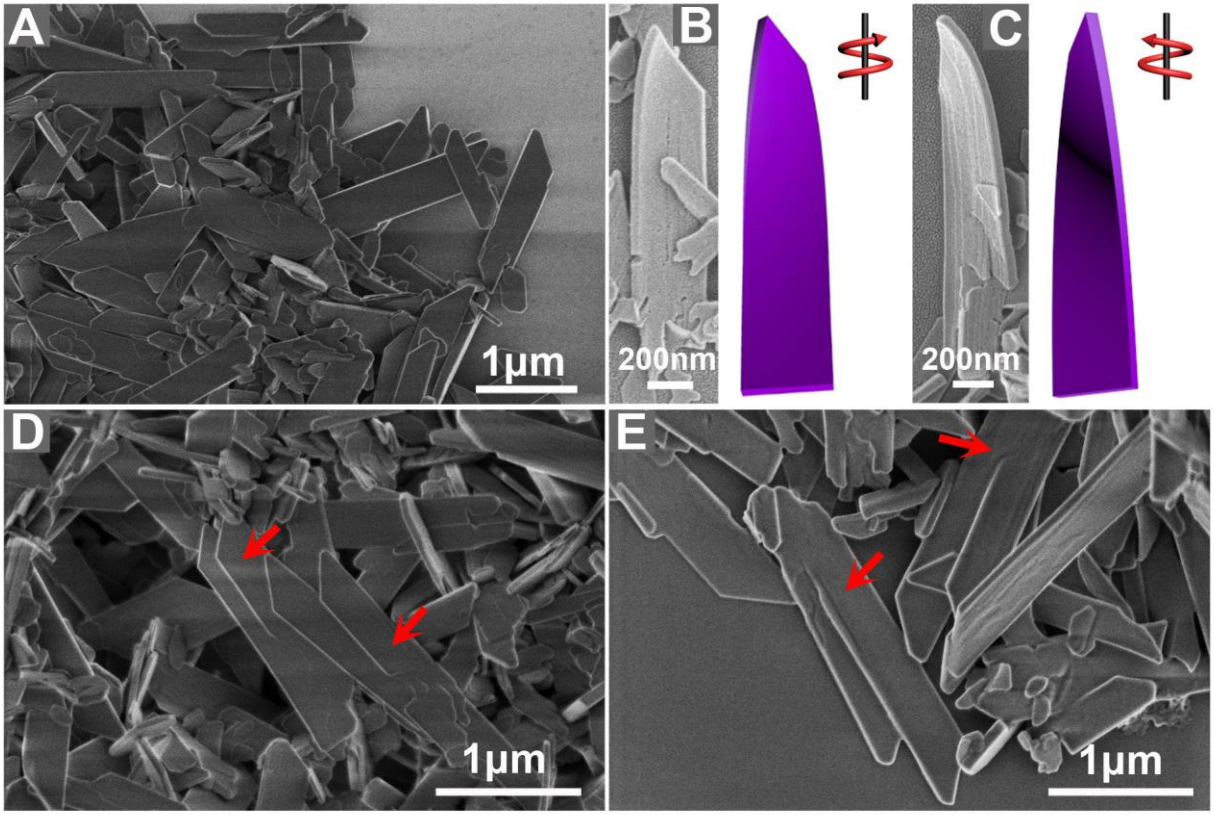

Figure S38. Morphology of Au/Ag-Cys assemblies. SEM images **A,** Au/Ag-*L*-Cys nanosheets with aspect ratio of ~5. The pitch length is so long that most of the sheets are flat under these conditions. **B,C,** Selected twisted ribbons from Au/Ag-*L*-Cys (B) and Au/Ag-*D*-Cys (C) samples; their pitch length can be estimated to be 10 µm. Similarly to HOPs from Au-*L*-Cys, Au/Ag-*L*-Cys twisted ribbons are right-handed, while Au/Ag-*D*-Cys are left-handed. **D,E,** Chirality to screw dislocations in the initial growth stages for Au/Ag-*L*-Cys (D) and Au/Ag-*D*-Cys (E), indicated by red arrows. The Ag-to-Au ratios are 16.5% and 17.4% in HOPs and synthetic solutions, respectively. The concentration of *L*-cysteine in solution was 104 mM during synthesis.

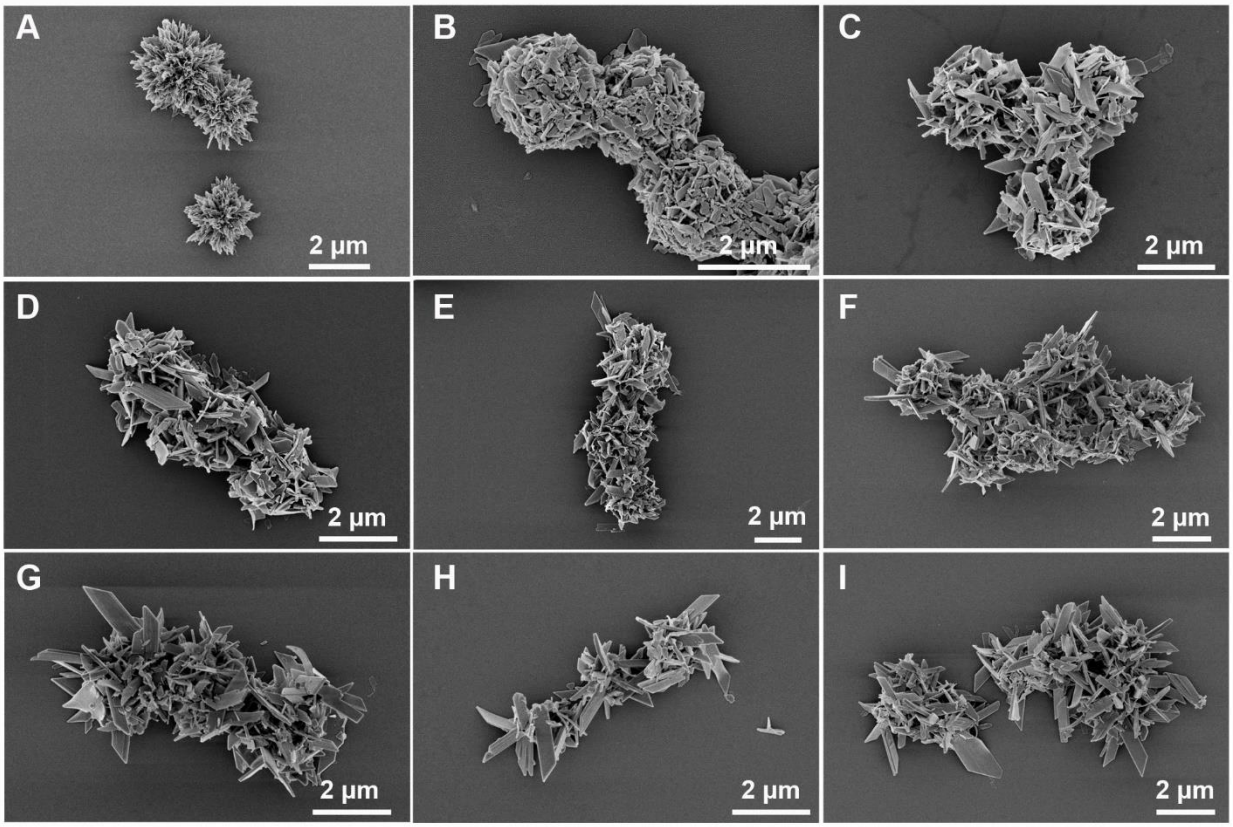

Figure S39. SEM images of Au/Ag-*L*-Cys HOPs and other assemblies doped with different amounts of silver. A to **I,** Into every 1 mL $HAuCl_4$/CTAB solution (17 μmol gold ions), the amount of silver ions added was: 0 (A), 0.59 (B), 1.18 (C), 1.77 (D), 2.35 (E), 2.94 (F), 3.53 (G), 4.12 (H), 4.71 (I) μmol. Corresponding Ag-Au molar ratio in the synthesis solution is 0%, 3.5%, 7.0%, 10.4%, 13.9%, 17.4%, 20.9%, 24.3%, 27.8%, respectively; the amount of *L*-Cys added was 0.114 mmol for all samples. The corresponding concentration of *L*-Cys was 114, 112, 110, 108, 106, 104, 102, 100 and 98 mM; the final volume of solution in each sample was different due to addition of different amounts of Ag salts and was equal to 1, 1.02, 1.04, 1.06, 1.08, 1.1, 1.12, 1.14 and 1.16 mL. With increasing amounts of silver, HOPs and spherical supraparticles gradually disappear and individual ribbons grow longer.

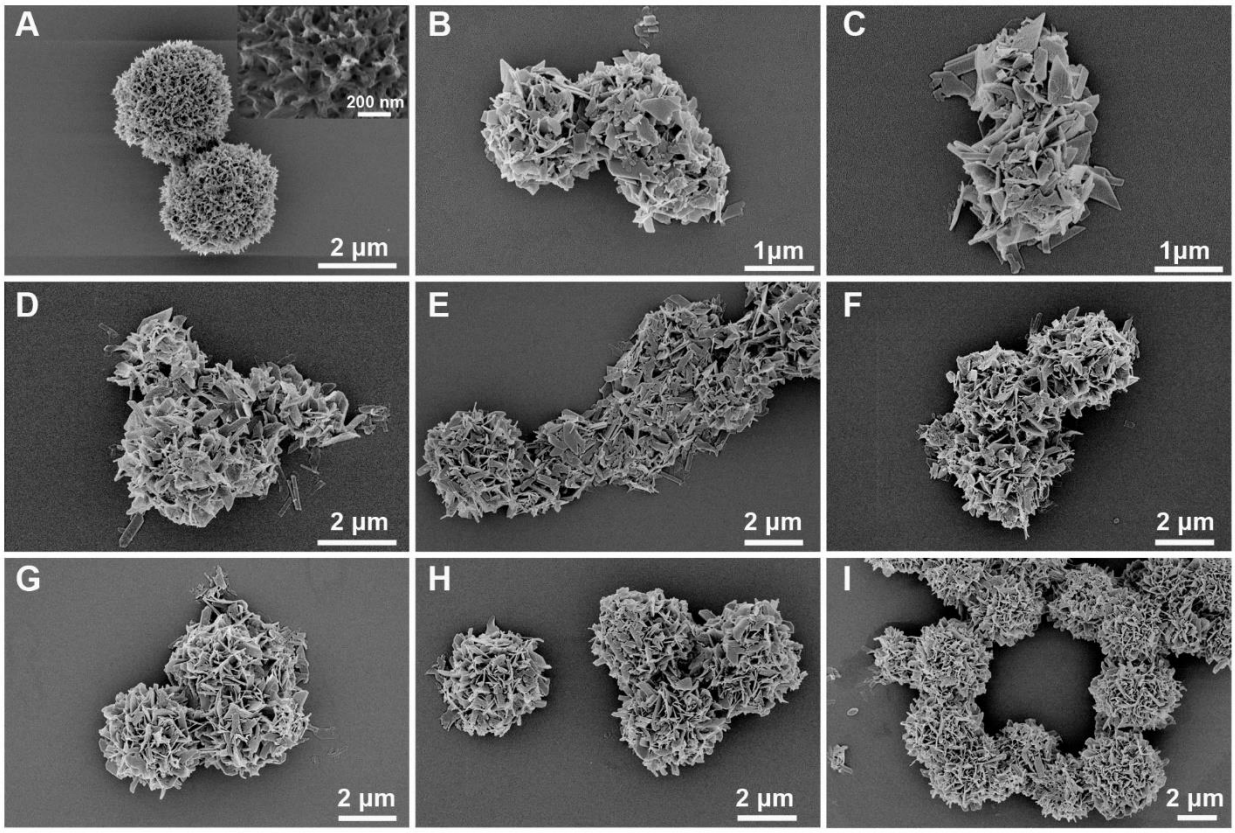

Figure S40. SEM images of Au/Ag-*L*-Cys prepared with different amount of *L*-cysteine. A to **I,** In each experimental series, a 1 mL $HAuCl_4$/CTAB solution was first mixed with 1.77 μmol silver nitrate so that the atomic ratio of Ag to Au would be 10.4%. Then different amounts of *L*-cysteine were added: 28.47 (A), 56.94 (B), 85.41 (C), 113.88 (D), 142.34 (E), 170.81 (F), 199.28 (G), 227.75 (H), 256.22 (I) μmol. The corresponding concentrations of *L*-Cys were 25.6, 49.1, 70.6, 90.4, 108.7, 125.6, 141.3, 156.0 and 169.7 mM, respectively. With increasing amounts of cysteine, spherical structures firstly decrease and then increase in diameter. Short spikes are predominantly observed rather than twisted ribbons, reflecting an increase of their stiffness and therefore elastic energy associated with their twisting.

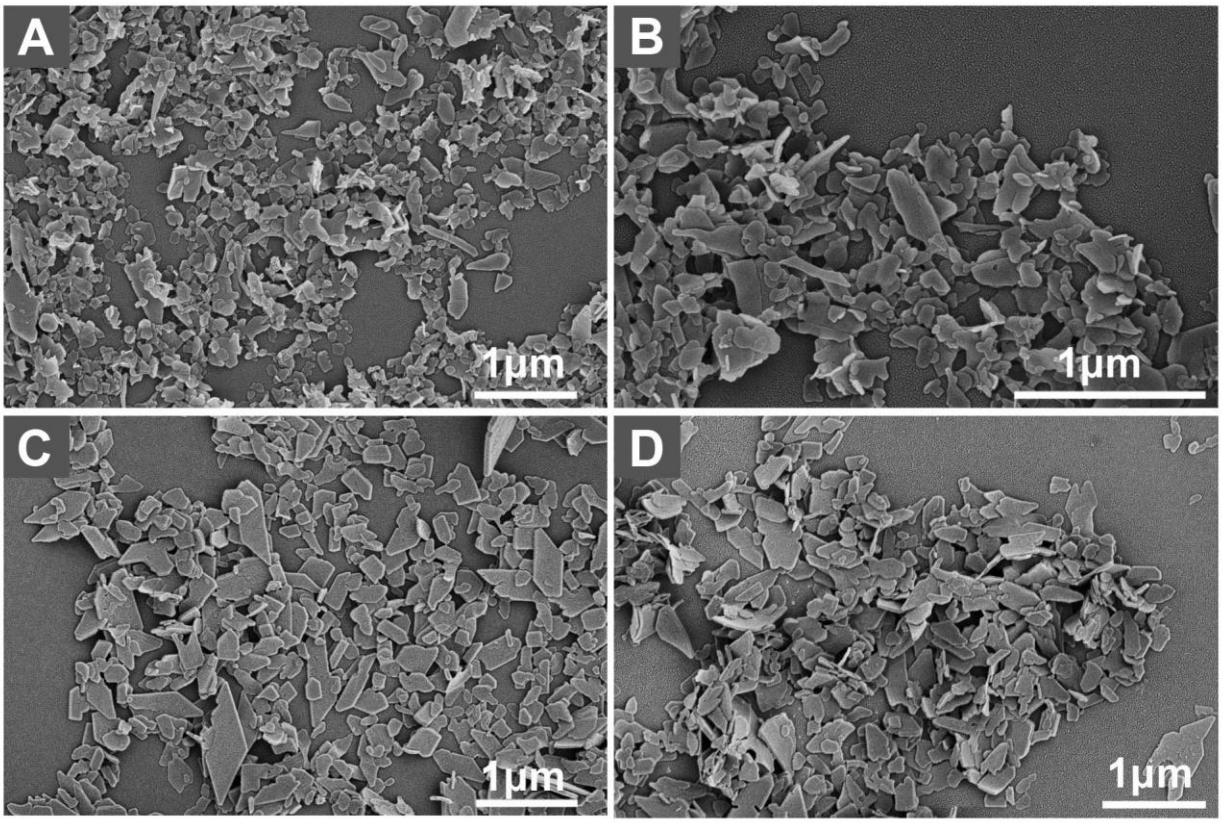

Figure S41. SEM images of Au/Cu-Cys and Au/Ag-Cys assemblies after sonication for 15 min. A, Au/Cu-*L*-Cys, **B,** Au/Cu-*D*-Cys, **C**, Au/Ag-*L*-Cys and **D**, Au/Ag-*D*-Cys assemblies.

Table S5. Luminescent quantum yields of different HOPs based on gold-cysteine chemistry.

Sample	Quantum Yield
Au-*L*-Cys	0.03
Au-*D*-Cys	0.03
Au/Ag-*L*-Cys	0.25
Au/Ag-*D*-Cys	0.24
Au/Cu-*L*-Cys	0.08
Au/Cu-*D*-Cys	0.06

Quantum yields were calculated by using quinine sulfate as a reference.

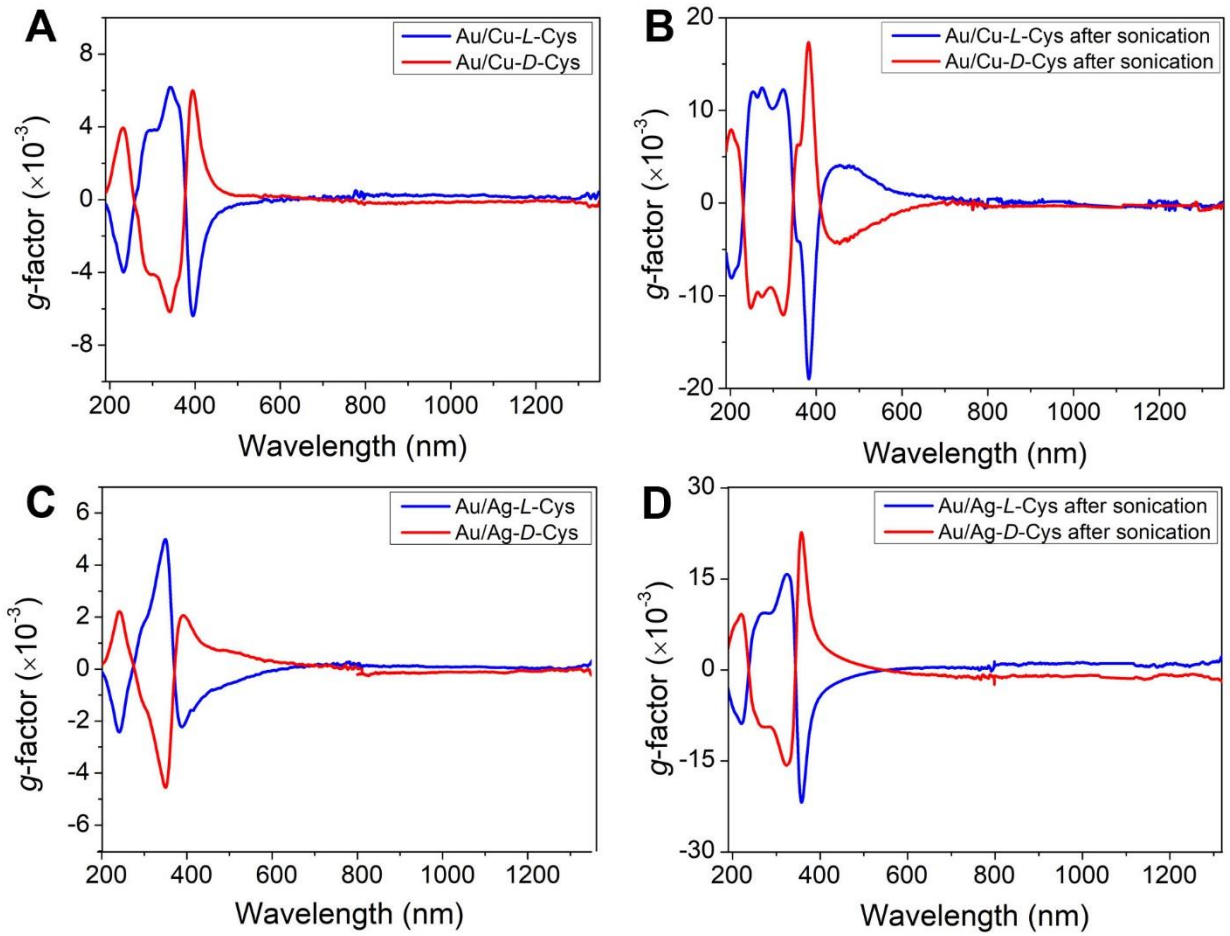

Figure S42. CD spectra of Au/Cu-Cys HOPs and Au/Ag-Cys twisted ribbons. A,B, *g*-factor of Au/Cu-Cys HOPs before (A) and after (B) sonication. **C,D,** *g*-factor of Au/Ag-Cys nanoribbons before (C) and after (D) sonication. Samples prepared with *L*-cysteine are plotted in blue and those prepared with *D*-cysteine are in red. The optical asymmetry *g*-factor increased after sonication because scattering and absorption have opposite contributions to CD in the UV region for HOP. For the same reason, no CD inversion is observed both in Au/Cu-Cys and Au/Ag-Cys assemblies in the 650-1350 nm spectral window.

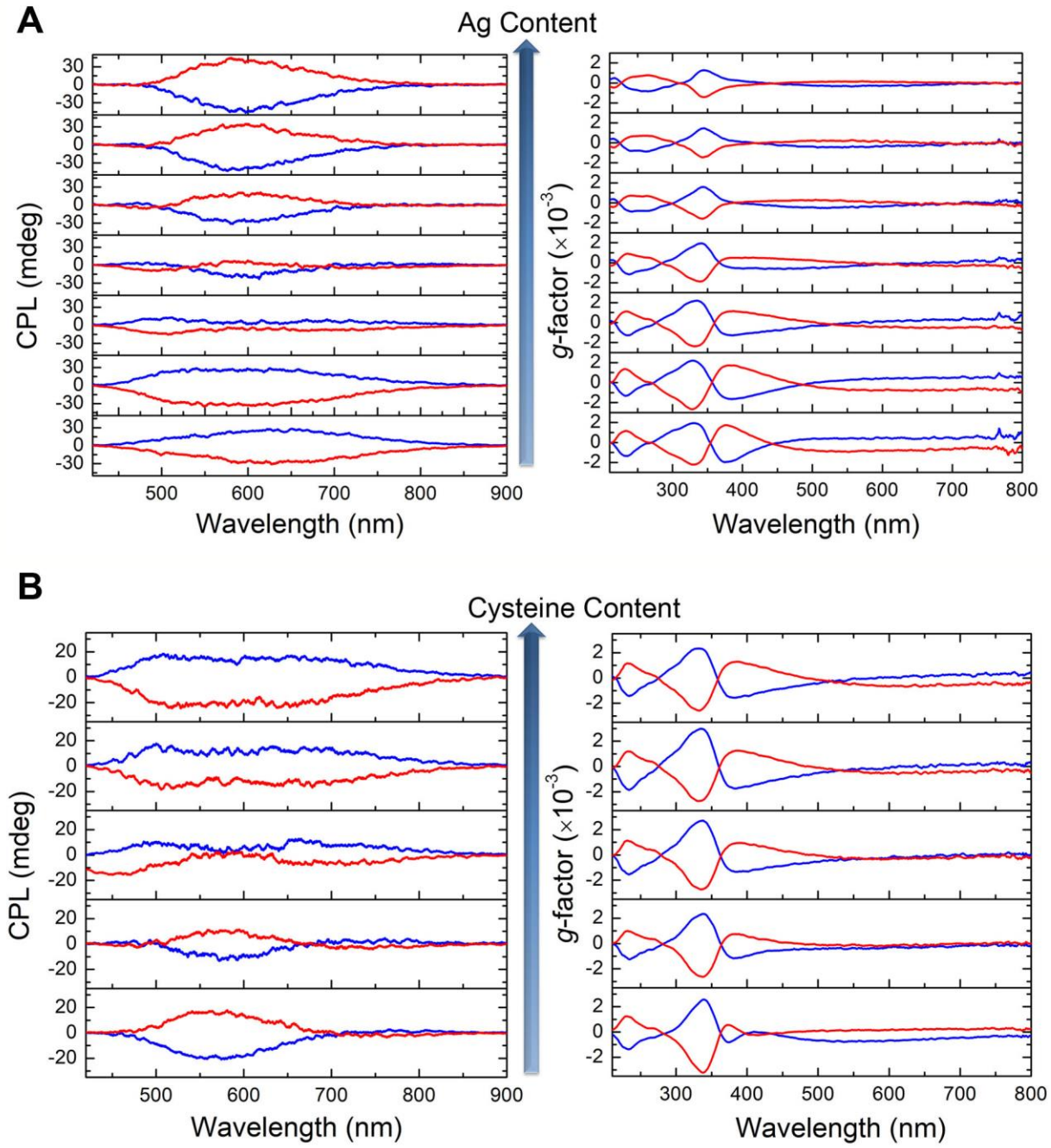

Figure S43. CPLE (left) and CD (right) spectra of Au/Ag-Cys superstructures with different amounts of silver (A) or cysteine (B). Samples prepared with *L*-cysteine are plotted in blue and those prepared with *D*-cysteine are in red.

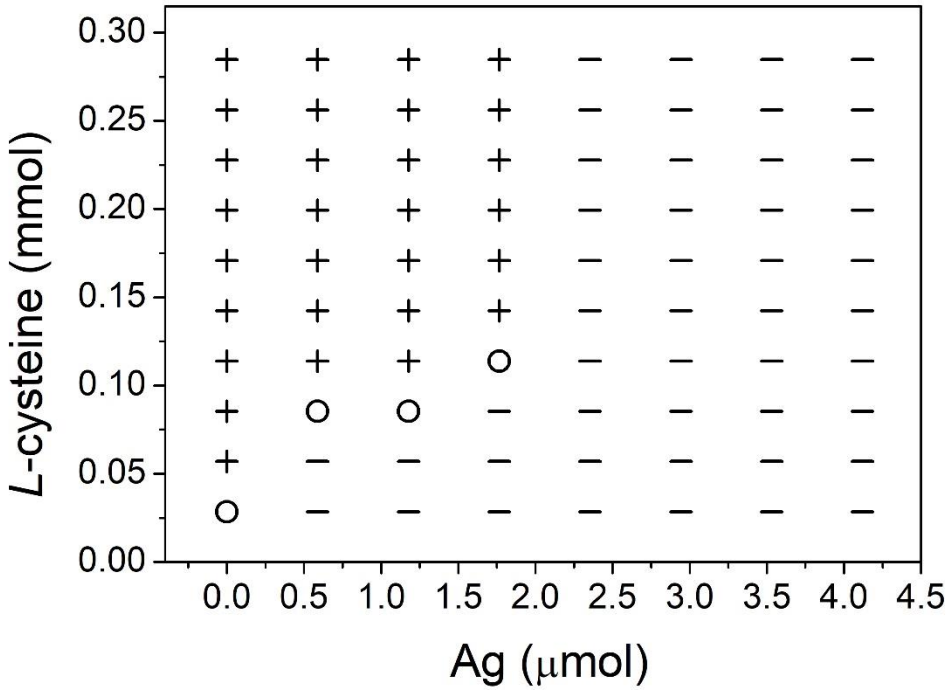

Figure S44. Dependence of the CPLE sign of Au/Ag-*L*-Cys HOPs on the amount of silver and cysteine added to 17 μmol $HAuCl_4$. CPLE sign: positive (+), negative (-) and neutral (o). Individual nanoribbons produced for high doping were also CPLE active. As the level of Ag doping increases, the sign of CPLE peak of Au/Ag-*L*-Cys gradually changed from positive to negative.

Movie S1.
Difference in Löwdin electronic population for each atom in the excited state as compared to the ground state.

Movie S2.
Molecular mechanics simulation of the computational twisting of Au-*L*-Cys nanoribbon used in calculation of the elastic and electrostatic interactions of Au-*L*-Cys nanoplatelets.

References

1. S.-H. Yu, H. Cölfen, K. Tauer, M. Antonietti, Tectonic arrangement of $BaCO_3$ nanocrystals into helices induced by a racemic block copolymer. *Nat. Mater.* **4**, 51–55 (2005). doi:10.1038/nmat1268 Medline

2. A. Gal, R. Wirth, J. Kopka, P. Fratzl, D. Faivre, A. Scheffel, Macromolecular recognition directs calcium ions to coccolith mineralization sites. *Science* **353**, 590–593 (2016). doi:10.1126/science.aaf7889 Medline

3. W. Jiang, M. S. Pacella, D. Athanasiadou, V. Nelea, H. Vali, R. M. Hazen, J. J. Gray, M. D. McKee, Chiral acidic amino acids induce chiral hierarchical structure in calcium carbonate. *Nat. Commun.* **8**, 15066 (2017). doi:10.1038/ncomms15066 Medline

4. H. E. Lee, H. Y. Ahn, J. Mun, Y. Y. Lee, M. Kim, N. H. Cho, K. Chang, W. S. Kim, J. Rho, K. T. Nam, Amino-acid- and peptide-directed synthesis of chiral plasmonic gold nanoparticles. *Nature* **556**, 360–365 (2018). doi:10.1038/s41586-018-0034-1 Medline

5. L. Zhang, T. Wang, Z. Shen, M. Liu, Chiral Nanoarchitectonics: Towards the Design, Self-Assembly, and Function of Nanoscale Chiral Twists and Helices. *Adv. Mater.* **28**, 1044–1059 (2016). doi:10.1002/adma.201502590 Medline

6. Y. Duan, X. Liu, L. Han, S. Asahina, D. Xu, Y. Cao, Y. Yao, S. Che, Optically active chiral CuO “nanoflowers”. *J. Am. Chem. Soc.* **136**, 7193–7196 (2014). doi:10.1021/ja500197e Medline

7. X. Liu, F. Zhang, X. Jing, M. Pan, P. Liu, W. Li, B. Zhu, J. Li, H. Chen, L. Wang, J. Lin, Y. Liu, D. Zhao, H. Yan, C. Fan, Complex silica composite nanomaterials templated with DNA origami. *Nature* **559**, 593–598 (2018). doi:10.1038/s41586-018-0332-7 Medline

8. S. Mann, G. A. Ozin, Synthesis of inorganic materials with complex form. *Nature* **382**, 313–318 (1996). doi:10.1038/382313a0

9. D. Deng, C. Hao, S. Sen, C. Xu, P. Král, N. A. Kotov, Template-Free Hierarchical Self-Assembly of Iron Diselenide Nanoparticles into Mesoscale Hedgehogs. *J. Am. Chem. Soc.* **139**, 16630–16639 (2017). doi:10.1021/jacs.7b07838 Medline

10. J. J. De Yoreo, P. U. P. A. Gilbert, N. A. J. M. Sommerdijk, R. L. Penn, S. Whitelam, D. Joester, H. Zhang, J. D. Rimer, A. Navrotsky, J. F. Banfield, A. F. Wallace, F. M. Michel, F. C. Meldrum, H. Cölfen, P. M. Dove, Crystallization by particle attachment in synthetic, biogenic, and geologic environments. *Science* **349**, aaa6760 (2015). doi:10.1126/science.aaa6760 Medline

11. S. Pieraccini, S. Masiero, A. Ferrarini, G. Piero Spada, Chirality transfer across length-scales in nematic liquid crystals: Fundamentals and applications. *Chem. Soc. Rev.* **40**, 258–271 (2011). doi:10.1039/B924962C Medline

12. P. Duan, H. Cao, L. Zhang, M. Liu, Gelation induced supramolecular chirality: Chirality transfer, amplification and application. *Soft Matter* **10**, 5428–5448 (2014). doi:10.1039/C4SM00507D Medline

13. T. Gibaud, E. Barry, M. J. Zakhary, M. Henglin, A. Ward, Y. Yang, C. Berciu, R. Oldenbourg, M. F. Hagan, D. Nicastro, R. B. Meyer, Z. Dogic, Reconfigurable self-assembly through chiral control of interfacial tension. *Nature* **481**, 348–351 (2012). doi:10.1038/nature10769 Medline

14. T. Aida, E. W. Meijer, S. I. Stupp, Functional supramolecular polymers. *Science* **335**, 813–817 (2012). doi:10.1126/science.1205962 Medline

15. T. Shimizu, M. Kogiso, M. Masuda, Vesicle assembly in microtubes. *Nature* **383**, 487–488 (1996). doi:10.1038/383487b0

16. I. Dolamic, B. Varnholt, T. Bürgi, Chirality transfer from gold nanocluster to adsorbate evidenced by vibrational circular dichroism. *Nat. Commun.* **6**, 7117 (2015). doi:10.1038/ncomms8117 Medline

17. C. Noguez, I. L. Garzón, Optically active metal nanoparticles. *Chem. Soc. Rev.* **38**, 757–771 (2009). doi:10.1039/b800404h Medline

18. S. Cha, J. Kim, K. Kim, J. Lee, Preparation and Photoluminescent Properties of Gold (I) - Alkanethiolate Complexes Having Highly Ordered Supramolecular Structures. *Chem. Mater.* **19**, 6297–6303 (2007). doi:10.1021/cm7024944

19. B. Söptei, J. Mihály, I. C. Szigyártó, A. Wacha, C. Németh, I. Bertóti, Z. May, P. Baranyai, I. E. Sajó, A. Bóta, The supramolecular chemistry of gold and L-cysteine: Formation of photoluminescent, orange-emitting assemblies with multilayer structure. *Colloids Surf. A* **470**, 8–14 (2015). doi:10.1016/j.colsurfa.2015.01.048

20. H. Nie, M. Li, Y. Hao, X. Wang, S. X.-A. Zhang, Time-resolved monitoring of dynamic self-assembly of Au(I)-thiolate coordination polymers. *Chem. Sci.* **4**, 1852 (2013). doi:10.1039/c3sc22215b

21. C. Li, K. Deng, Z. Tang, L. Jiang, Twisted metal-amino acid nanobelts: Chirality transcription from molecules to frameworks. *J. Am. Chem. Soc.* **132**, 8202–8209 (2010). doi:10.1021/ja102827f Medline

22. S. Grimme, C. Bannwarth, Ultra-fast computation of electronic spectra for large systems by tight-binding based simplified Tamm-Dancoff approximation (sTDA-xTB). *J. Chem. Phys.* **145**, 054103 (2016). doi:10.1063/1.4959605 Medline

23. Y. Xia, T. D. Nguyen, M. Yang, B. Lee, A. Santos, P. Podsiadlo, Z. Tang, S. C. Glotzer, N. A. Kotov, Self-assembly of self-limiting monodisperse supraparticles from polydisperse nanoparticles. *Nat. Nanotechnol.* **6**, 580–587 (2011). doi:10.1038/nnano.2011.121 Medline

24. G. M. Grason, Perspective: Geometrically frustrated assemblies. *J. Chem. Phys.* **145**, 110901 (2016). doi:10.1063/1.4962629

25. J. R. Young, J. M. Didymus, P. R. Brown, B. Prins, S. Mann, Crystal assembly and phylogenetic evolution in heterococcoliths. *Nature* **356**, 516–518 (1992). doi:10.1038/356516a0

26. W. Ma, H. Kuang, L. Wang, L. Xu, W.-S. Chang, H. Zhang, M. Sun, Y. Zhu, Y. Zhao, L. Liu, C. Xu, S. Link, N. A. Kotov, Chiral plasmonics of self-assembled nanorod dimers. *Sci. Rep.* **3**, 1934 (2013). doi:10.1038/srep01934 Medline

27. M. Sun, L. Xu, J. H. Bahng, H. Kuang, S. Alben, N. A. Kotov, C. Xu, Intracellular localization of nanoparticle dimers by chirality reversal. *Nat. Commun.* **8**, 1847 (2017). doi:10.1038/s41467-017-01337-2 Medline

28. H. Nie, M. Li, Y. Hao, X. Wang, S. Gao, P. Wang, B. Ju, S. X.-A. Zhang, Morphology modulation and application of Au(I)–thiolate nanostructures. *RSC Adv.* **4**, 50521–50528 (2014). doi:10.1039/C4RA06500J

29. J. H. Bahng, B. Yeom, Y. Wang, S. O. Tung, J. D. D. Hoff, N. Kotov, Anomalous dispersions of ‘hedgehog’ particles. *Nature* **517**, 596–599 (2015). doi:10.1038/nature14092 Medline

30. M. Liu, L. Zhang, T. Wang, Supramolecular Chirality in Self-Assembled Systems. *Chem. Rev.* **115**, 7304–7397 (2015). doi:10.1021/cr500671p Medline

31. S. R. Kirchner, M.-N. Su, J. H. Bahng, D. G. Montjoy, W.-S. Chang, N. A. Kotov, S. Link, Scattering Properties of Individual Hedgehog Particles. *J. Phys. Chem. C* **122**, 12015–12021 (2018). doi:10.1021/acs.jpcc.8b03823

32. J.-C. Chambron, C. Dietrich-Buchecker, J.-P. Sauvage, in *Supramolecular Chemistry I—Directed Synthesis and Molecular Recognition* (Springer, 1993), pp. 131–162.

33. M. Randic, D. Plavsic, On the concept of molecular complexity. *Croat. Chem. Acta* **75**, 107–116 (2002).

34. C. Gao, S. Kewalramani, D. M. Valencia, H. Li, J. M. McCourt, M. Olvera de la Cruz, M. J. Bedzyk, Electrostatic shape control of a charged molecular membrane from ribbon to scroll. *Proc. Natl. Acad. Sci. U.S.A.* **116**, 22030–22036 (2019). doi:10.1073/pnas.1913632116 Medline

35. E. Marino, D. M. Balazs, R. W. Crisp, D. Hermida-Merino, M. A. Loi, T. E. Kodger, P. Schall, Controlling Superstructure-Property Relationships via Critical Casimir Assembly of Quantum Dots. *J. Phys. Chem. C* **123**, 13451–13457 (2019). doi:10.1021/acs.jpcc.9b02033 Medline

36. W. Feng, J.-Y. Kim, X. Wang, H. A. Calcaterra, Z. Qu, L. Meshi, N. A. Kotov, Assembly of mesoscale helices with near-unity enantiomeric excess and light-matter interactions for

chiral semiconductors. *Sci. Adv.* **3**, e1601159 (2017). doi:10.1126/sciadv.1601159 Medline

37. G. I. Guerrero-García, E. González-Tovar, M. Olvera de la Cruz, Effects of the ionic size-asymmetry around a charged nanoparticle: Unequal charge neutralization and electrostatic screening. *Soft Matter* **6**, 2056 (2010). doi:10.1039/b924438g

38. N. Boon, G. I. Guerrero-García, R. van Roij, M. Olvera de la Cruz, Effective charges and virial pressure of concentrated macroion solutions. *Proc. Natl. Acad. Sci. U.S.A.* **112**, 9242–9246 (2015). doi:10.1073/pnas.1511798112 Medline

39. M. E. Fisher, The theory of equilibrium critical phenomena. *Rep. Prog. Phys.* **30**, 615–730 (1967). doi:10.1088/0034-4885/30/2/306

40. Z. B. Qu, W.-J. Feng, Y. Wang, F. Romanenko, N. A. Kotov, Diverse nanoassemblies of graphene quantum dots and their mineralogical counterparts. *Angew. Chem. Int. Ed.* (2019). doi:10.1002/anie.201908216 Medline

41. H. Chang, H. D. Jang, Controlled synthesis of porous particles via aerosol processing and their applications. *Adv. Powder Technol.* **25**, 32–42 (2014). doi:10.1016/j.apt.2013.11.004

42. H. Fan, F. Van Swol, Y. Lu, C. J. Brinker, Multiphased assembly of nanoporous silica particles. *J. Non-Cryst. Solids* **285**, 71–78 (2001). doi:10.1016/S0022-3093(01)00434-3

43. F. Caruso, R. A. Caruso, H. Möhwald, Nanoengineering of inorganic and hybrid hollow spheres by colloidal templating. *Science* **282**, 1111–1114 (1998). doi:10.1126/science.282.5391.1111 Medline

44. S. Rahmani, J. Budimir, M. Sejalon, M. Daurat, D. Aggad, E. Vivès, L. Raehm, M. Garcia, L. Lichon, M. Gary-Bobo, J.-O. Durand, C. Charnay, Large Pore Mesoporous Silica and Organosilica Nanoparticles for Pepstatin A Delivery in Breast Cancer Cells. *Molecules* **24**, 332 (2019). doi:10.3390/molecules24020332 Medline

45. M. Chirea, Electron transfer at gold nanostar assemblies: A study of shape stability and surface density influence. *Catalysts* **3**, 288–309 (2013). doi:10.3390/catal3010288

46. J. Yan, W. Feng, J.-Y. Kim, J. Lu, P. Kumar, Z. Mu, X. Wu, X. Mao, N. A. Kotov, Self-assembly of chiral nanoparticles into semiconductor helices with tunable near-infrared optical activity. *Chem. Mater.* **32**, 476–488 (2020). doi:10.1021/acs.chemmater.9b04143

47. S. Asahina, M. Suga, H. Takahashi, H. Young Jeong, C. Galeano, F. Schüth, O. Terasaki, Direct observation and analysis of yolk-shell materials using low-voltage high-resolution scanning electron microscopy: Nanometal-particles encapsulated in metal-oxide, carbon, and polymer. *APL Mater.* **2**, 113317 (2014). doi:10.1063/1.4902435

48. W. Pan, M. He, L. Zhang, Y. Hou, C. Chen, Interfacial engineering of graphene nanosheets at MgO particles for thermal conductivity enhancement of polymer composites. *Nanomaterials* **9**, 798 (2019). doi:10.3390/nano9050798 Medline

49. D. Rodríguez-Fernández, T. Altantzis, H. Heidari, S. Bals, L. M. Liz-Marzán, A protecting group approach toward synthesis of Au-silica Janus nanostars. *Chem. Commun.* **50**, 79–81 (2014). doi:10.1039/C3CC47531J Medline